

# Towards a fully physical representation of snow on Arctic sea ice using a 3D snow-atmosphere model

David N. Wagner<sup>1,2</sup>, David Clemens-Sewall<sup>3</sup>, Markus M. Frey<sup>4</sup>, Océane Hames<sup>1,2</sup>, Mahdi Jafari<sup>1</sup>, Amy R. Macfarlane<sup>1</sup>, Adrien Michel<sup>1,5</sup>, Martin Schneebeli<sup>1</sup>, Matthew D. Shupe<sup>6,7</sup>, Nander Wever<sup>1</sup>, and Michael Lehning<sup>1,2</sup>

<sup>1</sup>WSL Institute for Snow and Avalanche Research SLF, Davos, Switzerland

<sup>2</sup>CRYOS, School of Architecture, Civil and Environmental Engineering, EPFL, Lausanne, Switzerland

<sup>3</sup>Thayer School of Engineering, Dartmouth College, Hanover, NH, USA

<sup>4</sup>British Antarctic Survey – Natural Environment Research Council, Cambridge, UK

<sup>5</sup>Federal Office of Meteorology and Climatology MeteoSwiss, Geneva, Switzerland

<sup>6</sup>NOAA Physical Science Laboratory, Boulder, CO, USA

<sup>7</sup>Cooperative Institute for the Research in Environmental Sciences, University of Colorado Boulder, Boulder, CO, USA

## Key Points:

- A 3D-snow modeling setup including snow transport and temporally changing detailed snow properties was adjusted for Arctic sea ice.
- The model reproduces snow transport with high accuracy, and performed well in modelling the surface density with some uncertainty.
- The model will allow to investigate the insulating effect on spatial ice thermodynamics, especially in ridged areas.

---

Corresponding author: David N. Wagner, [wagner.david@posteo.net](mailto:wagner.david@posteo.net)

## Abstract

Snow plays a crucial role in the heat transfer between the ocean and atmosphere in sea ice due to its insulating properties. However, wind-induced transport causes the snow distribution to be inhomogeneous, as snow forms dunes and accumulates around pressure ridges, hence, leading to a heterogeneous underlying ice growth and melt. While models can help to understand the complex interactions of snow and sea ice, there is currently no 3D snow cover model that considers detailed temporally changing snow cover properties that affect the wind-induced redistribution of snow. This study presents the first application of the 3D-snow cover-atmosphere model ALPINE3D with the drifting snow module to Arctic sea ice. The model was calibrated and validated with measurements from the MOSAiC expedition. Wind fields used by the snow drift routine were generated with OpenFOAM which was forced by observations. A sensitivity analysis showed the impact of an increased fluid threshold on snow redistribution. The model performed well in simulating snow transport and mass fluxes, but underestimated erosion and poorly reproduced dune formation due to a missing dynamic mesh. The density was partially reproduced very well by the model, but uncertainties still exist in some cases. Comparing the surface snow density results with 1-D SNOWPACK simulations, ALPINE3D produced smaller differences but larger temporal variation in between setups. The study also investigated details of deposition and erosion using cross sections, showing good agreements of snow height differences between model and observations and revealing spatially high-resolution parameters such as age of deposited snow, density, and thermal conductivity.

## Plain Language Summary

Snow affects the exchange of heat between the ocean and atmosphere in sea ice. It can insulate the underlying ice and affect how it grows and melts, but it is distributed unevenly by wind because the ice is often heavily deformed and wind also produces dunes. We used a computer model to simulate the distribution of snow on Arctic sea ice. We tested the model by comparing its results with measurements from the MOSAiC expedition. We found that the model performed well in simulating how snow is transported, but it underestimated erosion and was not able to accurately reproduce dune formation. ALPINE3D also computed the surface snow density, which showed at times good agreements with observations, but there are still some uncertainties. We compared the results with 1-D simulations from a model called SNOWPACK, and different ALPINE3D setups produced smaller differences in the end but a larger variation with time. The study also investigated details of deposition and erosion using cross sections, showing good agreements of snow height differences between model and observations and revealing information about snow age, density, and thermal conductivity. Overall, this study provides new insights into the complex interactions of snow and sea ice.

## 1 Introduction

The snow cover on Arctic sea ice forms a central element in the heat balance between the ocean and the atmosphere. On average, the snow cover in this area usually does not exceed 30 cm (Sturm et al., 2002; Wagner et al., 2022). However, due to its very high insulating capacity and high albedo, it may regulate the timing and speed of ice growth in autumn and winter, and melt in spring and summer (Nicolaus et al., 2006; Persson, 2012; Sturm & Massom, 2016). It further inhibits or delays ice melt during occasional warm-air intrusions that may occur even in winter (Persson et al., 2017).

Snow transport – the movement of snow particles due to wind – is initiated when a certain wind speed threshold is exceeded. This threshold depends on various processes, but mainly on vertical transport of horizontal momentum from the wind towards the surface and on the weight and the inter-granular bond strength of the snow grains. When

71 this threshold is exceeded, grains may start to creep, going into saltation or suspension  
72 mode when wind speeds are higher (Bagnold, 1941; R. A. Schmidt, 1980; Melo et al., 2021).

73 Where wind speeds are lower, net deposition of the grains may occur and leading  
74 to surface accumulation. These drifts occur in the form of dunes (Filhol & Sturm, 2015)  
75 - or around obstacles. On sea ice, these obstacles are mostly pressure ridges formed by  
76 differential ice motion (Liston & Elder, 2006a). On a small scale, these drifts may de-  
77 termine how the ice grows and melts locally, e.g. they may modify the formation of melt  
78 ponds (Petrich et al., 2012; Lecomte et al., 2015). The snow cover and snow transport  
79 over sea ice have been investigated several times in the past. Déry and Tremblay (2004)  
80 modeled blowing snow transport including blowing snow sublimation over sea ice with  
81 the PIEKTUK model and focused on the effect of snow mass loss into leads on the mass  
82 balance. However, Déry and Tremblay (2004) did not make use of a saltation model, prob-  
83 ably strongly underestimating horizontal mass fluxes. Leonard and Maksym (2011) mod-  
84 eled snow transport with the PIEKTUK model, as well, but with a saltation model in  
85 addition. The saltation transport threshold wind speed in this case was used as by Li  
86 and Pomeroy (1997), which is exclusively a function of the ambient temperature. Ele-  
87 vated temperatures lead to rapid sintering of the snow (i.e. increased formation of bonds  
88 between the snow grains) (Colbeck et al., 1997; Colbeck, 1998; Blackford, 2007) and there-  
89 fore an increased threshold of wind-induced snow transport. The saltating mass flux it-  
90 self is computed with the model from Pomeroy and Gray (1990). However, (Melo et al.,  
91 2021) showed in a model-intercomparison that this model underestimated the integrated  
92 mass flux significantly.

93 Liston et al. (2018, 2020) modeled snow transport in a very detailed way with their  
94 SnowModel, with statistically computed 2D-wind fields (Liston & Elder, 2006b) and a  
95 bulk-density snow cover representation. The core model for snow redistribution within  
96 SnowModel is SnowTran-3D (Liston & Sturm, 1998; Liston et al., 2007), whose thresh-  
97 old friction velocity is exclusively a function of a constant snow density (Liston et al.,  
98 2007). Liston et al. (2007) argue that this simple approach was sufficient for very low  
99 temperatures in winter in their studies, since a nearly constant surface-shear strength  
100 for the snow occurred under these conditions. However, they included the caveat that  
101 this approach may reach its limits for higher temperatures and detailed developments  
102 during snowstorms when more complex ambient conditions arise. SNOWPACK, a 1-D  
103 snow cover model applied recently to sea ice (Lehning et al., 1999; Wever et al., 2020),  
104 uses a saltation model to simulate snow transport if needed, which takes into account  
105 the surface properties of the temporally changing snow microstructure as well as the snow  
106 density (Doorschot & Lehning, 2002). Therefore, we believe that this approach could pro-  
107 vide an advantage when studying snow cover on Arctic sea ice in a warming climate in-  
108 cluding warm air intrusions in winter, as well as during warmer months. In a saltation  
109 model inter-comparison, Melo et al. (2021) could show that with respect to integrated  
110 mass flux, the model from Doorschot and Lehning (2002) performed well for the tested  
111 specific bed types.

112 SNOWPACK has been applied in a distributed way in the form of ALPINE3D (Lehning  
113 et al., 2006), mostly for the Alps (Mott et al., 2010; Gerber et al., 2017; Schlögl et al.,  
114 2016), but for sea ice, as well (Wever et al., 2021). However, Wever et al. (2021) did not  
115 run the model with snow transport, i.e. without the SnowDrift module as presented in  
116 Lehning et al. (2008). Another approach recently applied to a sea ice topography was  
117 modelling snow transport with a gas-particle two-phase turbulent flow solver (Hames et  
118 al., 2022). While the results regarding the locations of erosion and deposition are gen-  
119 erally promising, no temporal evolution of the physical parameters of the snowpack is  
120 implemented in the model, which however would change the fluid threshold with time  
121 - relevant snow bed parameters are set to constant and sintering effects due to temper-  
122 ature are not considered. In addition, erosional or depositional changes of the snow cover  
123 are solely computed with respect to mass.

As already mentioned, ALPINE3D was mainly applied for larger Alpine scale simulations in the past. However, snow processes on sea ice are in principle not different than snow processes that occur in mountains, and there are only few snow models that are capable to conduct detailed snow transport modeling at this time. Hence, we built upon these previous studies by combining individual state-of-the-art methods as a novel approach of modeling of snow on sea ice, which – to our knowledge – has not been used in any other model setup so far:

- Detailed spatial modeling of the snow cover with very high resolution ( $dx, dy = 0.35$  m) by means of SNOWPACK/ALPINE3D (Lehning et al., 1999, 2006).
- modeling snow saltation (Doorschot et al., 2004), suspension, erosion and deposition with ALPINE3D based on high-resolution Reynolds-averaged Navier-Stokes (RANS) equations based wind fields modeled with OpenFOAM (Weller et al., 1998).
- Making use of a very detailed digital elevation model (DEM) based on terrestrial laser scans (TLS) collected during the Multidisciplinary drifting Observatory for the Study of Arctic Climate (MOSAiC) expedition (Nicolaus et al., 2021) to have a realistic initial grid.
- Force the models with a detailed dataset of measured atmospheric parameters during the MOSAiC field campaign (Shupe et al., 2022).
- Validate the model with highly detailed spatial measurements of the height and density of the snow cover collected during MOSAiC as described in Nicolaus et al. (2021) and Wagner et al. (2022).

The goals of our study are to:

1. Calibrate and validate the model setup for the given conditions on sea ice during polar night.
2. Investigate snow re-distribution from a statistical point of view.
3. Investigate how a changed snow transport threshold may lead to a change of transport rates and therefore a change in deposition/erosion patterns.
4. Evaluate the modeled snow surface density.
5. Compare with a 1-D modelling approach.

## 2 Methods and Data

### 2.1 Area and time selection

Snow- and atmospheric data was collected during the MOSAiC expedition (Nicolaus et al., 2021; Shupe et al., 2022) on sea ice in the high Arctic.

The exact study area on the ice floe and the time period were selected based on available observations that can be used to drive and evaluate the model. We also ensured that at least one drifting snow event occurred within this time period and TLS before and after the period were conducted, which required calm conditions. In addition, the topography in the study area should be sufficiently uneven in order for snow to accumulate. Hence, we decided for the 10-day long time period 25 Jan – 4 Feb 2020 (Fig. 1) covering the area of the northern transect (Fig. 2, a fixed track, which crossed an area consisting of second-year ice (SYI), on which snow depth measurements were taken weekly with high spatial resolution using a Magnaprobe (Sturm & Holmgren, 2018; Itkin et al., 2021; Nicolaus et al., 2021; Wagner et al., 2022)). Within this period, 4 more distinct drifting snow occurred, marked in yellow in Fig. 1. For this period, continuous meteorological measurements were available (Shupe et al., 2021, 2022), as well as one TLS on 25 Jan and one on 4 Feb for the northern transect area. In addition, occasional detailed snow cover and transect snow depth measurements were available for this area and period (Fig. 2). Based on drifting snow measurements with the snow particle counter (SPC)

172 installed on the flux tower that was installed in the MOSAiC Central Observatory (Shupe  
173 et al., 2022) at 0.1 m above the snow surface we could determine the drifting snow pe-  
174 riods. Detailed descriptions of the flux tower setup and snow measurements follow in a  
175 later section. In Fig. 1d, it can well be seen that one TLS was conducted on 25 Jan 2020  
176 before the start of the drifting snow period and one after the drifting snow periods on  
177 4 Feb 2020. The initial scan on 25 Jan 2020 was used to produce digital elevation mod-  
178 els (DEMs) to be used as lower boundary topography for the model. The vertical dif-  
179 ference between both scans is used to evaluate snow height distribution differences found  
180 in the simulations. It should precede the rest of the manuscript, that the conditions with  
181 4 drifting snow events under different wind directions are not ideal for a calibration of  
182 the model, however, the aggravated conditions on the moving ice (Nicolaus et al., 2021)  
183 have to be taken into account, which rarely allowed for a referencing of the TLS at dif-  
184 ferent days. We have been able to investigate two of these rare days here.

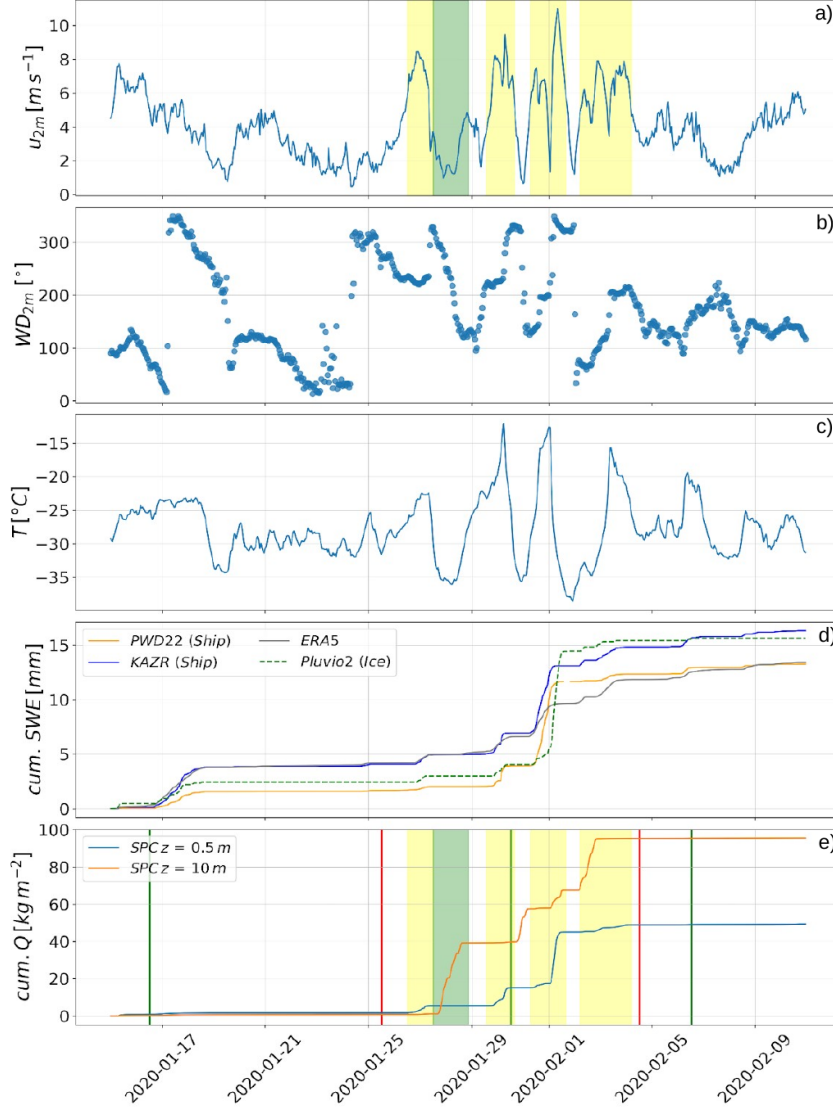


**Figure 1.** Time series of measured parameters between 16 Jan and 10 Feb 2020, for a) wind speed measured at 2 m height on the flux tower, b) wind direction with respect to the wind speed shown in a), c) 2 m air temperature at the flux tower, d) cumulative precipitation sums measured on the ship-based optical PWD22 sensor, retrieved from the  $K_a$ -Band Radar on the ship, ERA-5 reanalysis snowfall, Pluvio<sup>2</sup> pluviometer measured snowfall on the ice and e) cumulative horizontal mass flux for the snow particle counters (SPCs) on the flux tower, measured at 0.1 m and 10 m height, respectively. The green vertical lines in e) mark the days where transect measurements were conducted and the red vertical lines mark the days on which TLS were conducted in the same area. The yellow shaded areas in a) and e) mark the time periods of the drifting snow events. The green shaded area mark a suspicious increase of mass flux at the SPC installed at 10 m while wind speeds would theoretically not allow for snow transport. More details about snowfall measurements- and retrieval and SPC measurements can be found in Shupe et al. (2021); Wagner et al. (2022); Matrosov et al. (2022); Shupe et al. (2022).

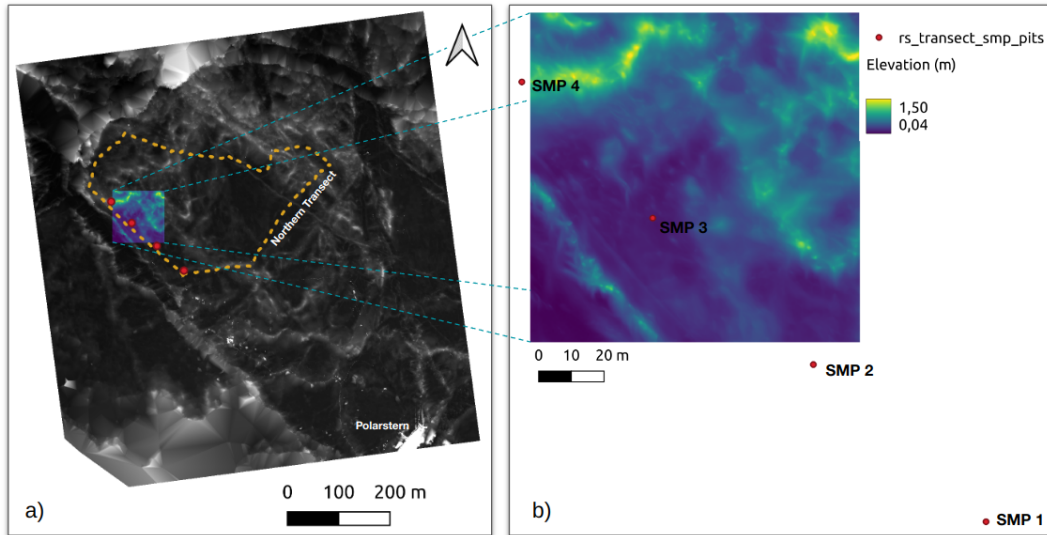


**Figure 2.** a) Shows the DEM derived from TLS on floe-scale, with the embedded model-domain. It also covers the northern transect and the location of FS Polarstern in the lower left corner. b) Shows the DEM on a smaller scale, including elevation magnitude and snow pit locations 1 – 4, where weekly SMP measurements were conducted.

185

## 2.2 DEM processing

186

187

188

189

190

191

192

193

194

195

196

197

198

199

200

201

202

203

TLS data was collected during the MOSAiC field campaign. Scans were conducted on 25 Jan and 4 Feb 2020 and referenced to obtain one large point cloud for each day in the same coordinate system (Clemens-Sewall et al., 2023). A cloth simulation filter (Zhang et al., 2016) was applied to the surface with CloudCompare (2023), in order to remove artefacts like flags, persons, tents or machines from the point clouds. In the following, the points were rasterized to a resolution of  $\Delta x = \Delta y = \Delta z = 0.1$  m in order to obtain a digital elevation model using the SAGA Geographical Information System (Conrad et al., 2015). Afterward, gaps were closed with spline interpolation, followed by applying a filter to remove further non-ground cells (Vosselman, 2000). Subsequently, a multilevel B-spline interpolation (Lee et al., 1997) and a multi direction lee filter (Selige et al., 2006) were applied in order to smooth the surface. These steps are essential in order to remove sharp edges that might lead to issues with grid generation or numerical instabilities in either OpenFOAM or ALPINE3D. The DEMs were aligned with respect to true north and squares with side lengths of 200 by 200 m were cut out. DEMs as shown for the TLS observation on 25 Jan 2020 (Fig. 2) were obtained. The lowest point in the DEM on 25 Jan was set to zero reference for all surrounding cells and also for the second scan on 4 Feb 2020. The DEMs show generally heterogeneous elevation, with a maximum height of 1.8 m on the highest ridges.

204

## 2.3 OpenFOAM wind field modeling

205

### 2.3.1 Mesh setup

206

207

208

209

210

211

Before the actual meshing, a horizontal flat buffer zone of 20 m width was added at each side with a smooth transition into the domain with the approach from Hames et al. (2022). This is necessary to avoid numerical instabilities under periodic boundary conditions. Afterwards, similar to Hames et al. (2022), to border the domain for the mesh, walls of 25 m height were added to each side and a top was added. Within these borders, a cartesian terrain-following mesh was generated using the cfMesh open source library

212 (Juretic et al., 2021) for OpenFOAM. The mesh consists of polyhedral cells in the tran-  
 213 sition regions where cell sizes are different and of hexahedral cells in the regions where  
 214 cells sizes do not change anymore. The first layer above the ground has a height of 0.05 m,  
 215 and the layer spacing as well as the horizontal cell size increases gradually with the dis-  
 216 tance from the ground. Further above, the cell size was set to  $\Delta x$ ,  $\Delta y$ ,  $\Delta z = 1$  m. Even  
 217 if 1 m seems relatively large, it should be sufficient for the low-turbulence areas well above  
 218 the surface. The approach provided stable solutions and also has a lower computational  
 219 cost. For the lateral boundaries, the patches were set to a cyclic Arbitrary Mesh Inter-  
 220 face (AMI), which represents periodic boundary conditions.

### 221 **2.3.2 OpenFOAM model settings and parameters**

222 For wind field modeling, we used OpenFOAM® v2106 with the simpleFoam solver,  
 223 which is solving the continuity and momentum equations for in-compressible, turbulent  
 224 flow until a steady-state is obtained. To force the model, we used measured 1 h average  
 225 wind data at 10 m height above the ice from the flux tower, for the time period 26 Jan  
 226 – 4 Feb 2020. For each hour, that means one time step, 1 h average  $u$ ,  $v$  and  $w$  compo-  
 227 nents from 10 m were written into the OpenFOAM fvOption file as velocity which is trans-  
 228 lated into volume-averaged momentum source by the model. Hence, for each hour, an  
 229 OpenFOAM simulation is ran until steady state of the vector field is reached. With this  
 230 approach, short-term wind peaks, which certainly give strong impulses for the initiation  
 231 of snow transport, are averaged out - however, we see this as the only reasonable approach  
 232 if we want to calculate the snow transport itself in ALPINE3D also in hourly time steps.  
 233 Once a steady-state solution is found for the domain-wide wind field, a new simulation  
 234 starts with a new domain-averaged target wind vector. Thus we obtained a 3-D wind  
 235 field for each hour. Additionally, we determined a constant roughness length of  $z_0 = 5 \cdot$   
 236  $10^{-3}$  m as target roughness length in the model for the wall functions at the lower bound-  
 237 ary for turbulent dissipation rate  $\epsilon$  ( $\text{kg}^2 \text{s}^{-3}$ ) and turbulent viscosity  $\nu_t$  ( $\text{m}^2 \text{s}^{-1}$ ), by com-  
 238 paring measured with modeled wind profiles and reducing its error (Fig. 3). Note that  
 239 the comparison is limited, as we compare the horizontally averaged (height above the  
 240 surface per layer) wind from the model with point measurements at the flux tower. The  
 241 tower is not covered by the TLS scans (and therefore the model domain) for this period,  
 242 it was located approximately 750 m south-east from the center of the domain. Further-  
 243 more, due to strong motion of the ice, the tower was quickly surrounded by high pres-  
 244 sure ridges that affected the wind field. In addition, a hut was set up to the north-west,  
 245 where the measurement data from various instruments were collected and pre-processed.  
 246 Nonetheless, Weiss et al. (2011) found a median  $z_0$  of  $4.1 \cdot 10^{-3}$  m for Antarctic pack  
 247 ice and  $10^{-4}$  m for young ice, which is close to the obtained values from our compari-  
 248 son.

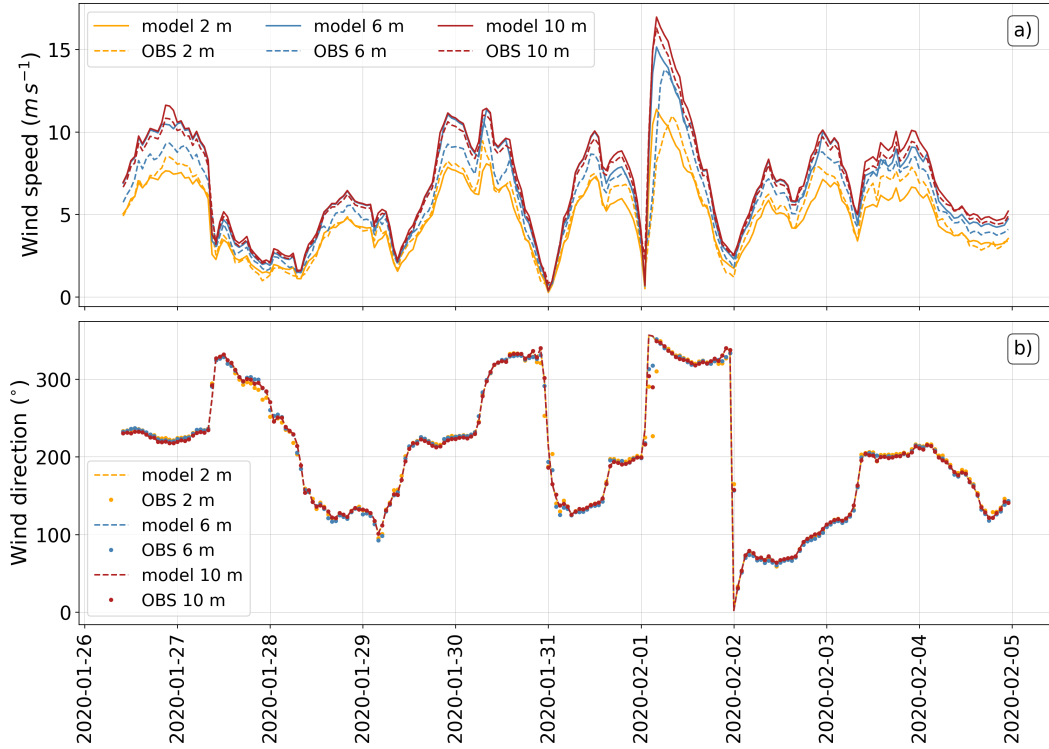


**Figure 3.** Comparison of wind measurements at the tower versus horizontally averaged model wind over time at the heights 2 m, 6 m and 10 m above the ice for a) wind speed and b) wind direction.

249

## 2.4 Snow cover and snow transport modeling

250

251

252

253

254

255

In order to conduct the actual snow cover- and transport modeling, we applied ALPINE3D (Lehning et al., 2008), which is a snow-atmosphere model using the 1-D layered SNOWPACK model for simulating the snow cover at each grid point (Lehning et al., 1999; Bartelt & Lehning, 2002). ALPINE3D enables to exchange surface mass fluxes and sublimation laterally between the connected grid cells. Its adjusted setup for sea ice is described in the following.

256

### 2.4.1 Meshing and wind field interpolation

257

258

259

260

261

262

263

264

265

266

267

268

As ALPINE3D requires a grid with hexa-hedral cells (Lehning et al., 2006, 2008), a new grid was required to be generated from the OpenFOAM unstructured mesh. To achieve this, we made use of the TerrainBlockMesher tool for OpenFOAM (J. Schmidt, 2014). By choosing cell increments (here:  $\Delta x, \Delta y = 0.35$  m), a vertical spacing of 0.2 m close to the surface with an exponential increase and a vertical extent of  $h(z) = 25$  m, TerrainBlockMesher reads the DEM of the sea ice and generates a structured grid on top which follows the terrain. The 3D wind fields from OpenFOAM were interpolated onto this structured grid with a Gaussian interpolation kernel by means of the PyVista Python library (Sullivan & Kaszynski, 2019). To run ALPINE3D, we chose a sub-section of the original DEM as shown in Fig. 2, a square with a side length of 100 by 100 m and a domain height reduced to 13 m which led to a 4-fold reduction in computation time when compared with the original domain size.

269

### 2.4.2 General model settings and parameters

270

271

272

273

274

275

276

The whole functionality of ALPINE3D is described in detail in Lehning et al. (2006, 2008). For saltation modeling, we applied the ALPINE3D-integrated saltation model from Doorschot and Lehning (2002). Although ALPINE3D's snowdrift routine is capable of computing sublimation of snow in suspension, we switched off that option, after finding only negligible differences. The reason is the small horizontal extent of the domain and the short time-span of the model run, leading to negligible snow mass sublimation in suspension for the meteorological conditions for the given time and location.

277

### 2.4.3 Meteorological Forcing

278

279

280

281

282

283

284

285

286

287

288

289

290

Besides the already described wind velocities, measurements of air temperature (measured at the flux tower at 2 m height), relative humidity with respect to ice (measured at the flux tower at 2 m height), precipitation rate ( $\text{mm h}^{-1}$ ) as retrieved from the  $K_a$ -band zenith radar (KAZR) installed on research vessel (RV) *Polarstern*, and incoming longwave radiation, measured near the flux tower, were used in the model. Note that no shortwave radiation input was required, as the research time period was during the polar night, without any incoming and outgoing shortwave radiation. General information about the MOSAiC atmospheric measurement setup including flux tower, radiation measurements, and KAZR can be found in Shupe et al. (2021, 2022). Detailed information about the KAZR can be found in Widener et al. (2012) while KAZR data can be found under Lindenmaier et al. (2020). The KAZR retrieval used in this paper follows Matrosov (2007); Matrosov et al. (2008) was applied by Wagner et al. (2022) and later evaluated by Matrosov et al. (2022) in detail.

291

### 2.4.4 Deposited snow density and microstructure

292

293

294

295

296

Regardless of whether it is new snow or previously eroded and redeposited snow, SNOWPACK uses the same parameterization for both density and microstructure with respect to this deposited snow. These parameters are calculated in ALPINE3D for each cell individually, mainly depending on the wind speed. For the deposited snow density  $\rho_n$ , we applied the following formula, adapted from Groot Zwaaftink et al. (2013)

$$\rho_n = \begin{cases} \rho_1 \cdot \log_{10}(U) + \rho_0, & \text{if } U \geq 1 \\ 33, & \text{otherwise} \end{cases} \quad (1)$$

297

298

299

300

301

where  $U$  is the instantaneous wind speed at a grid cell. For  $\rho_1$  we set  $361 \text{ kg m}^{-3}$  as in Groot Zwaaftink et al. (2013) and  $\rho_0 = 33 \text{ kg m}^{-3}$  in order to allow low snow densities at very low wind speeds. Contrary to Groot Zwaaftink et al. (2013), we also did not apply long-term averaged wind speeds in the formula but instantaneous wind speeds at each grid cell.

302

303

304

We further applied the POLAR variant of SNOWPACK which comes along with further surface compaction mechanics due to wind and changes in the snow settling which are described in Groot Zwaaftink et al. (2013); Steger et al. (2017).

305

306

307

308

309

310

311

312

313

For the deposited snow microstructure, in the POLAR variant, compared against the DEFAULT variant, various deposited snow properties differ, partially depending on the wind speed. In general (independently of the wind speed), the new snow sphericity is increased (0.75) compared to the DEFAULT variant (0.5), while the dendricity is decreased (0.5 vs. 1.0). At high wind speeds ( $> 5 \text{ m s}^{-1}$ ), the sphericity is increased even further (1.0 vs. 0.75) while the dendricity is decreased further (0.15 vs. 0.5), reflecting mechanical destruction of grains from transport by wind. Further, new snow bond size gets stronger with a factor of 3 compared to the DEFAULT variant. The POLAR variant also exhibits a stronger compaction of the near surface layers by wind, by applying

314 a magnifying factor. In addition, we applied a factor of 5 that is multiplied in addition  
 315 to favor wind slab formation.

#### 316 **2.4.5 Fluid threshold**

The drifting snow routine from ALPINE3D (Doorschot & Lehning, 2002) is computing drifting snow mass flux based on a fluid threshold shear stress initiating snow grain motion  $\tau_{th}$  (Pa) determined as:

$$\tau_{th} = A \rho_i g r_g (\psi + 1) + B \sigma N_3 \frac{r_b^2}{r_g^2} \quad (2)$$

317 where  $A = 0.023$  and  $B = 0.0035$  are empirically determined constants (Clifton et al.,  
 318 2006),  $\rho_i = 917 \text{ (kg m}^{-3}\text{)}$  is the density of ice,  $g = 9.81 \text{ (m s}^{-2}\text{)}$  is the gravitational ac-  
 319 celeration,  $r_g$  is the grain radius in m,  $r_b$  is the bond radius in m,  $\psi$  is the sphericity of  
 320 snow grains which can be between 0 and 1,  $\sigma = 300 \text{ (Pa)}$  is an empirically determined  
 321 bond strength and  $N_3$  is the three-dimensional coordination number.

The threshold friction velocity which must be exceeded by the wind at the surface to initiate snow transport is defined as:

$$u^*_{th} = \sqrt{\frac{\tau_{th}}{\rho_a}}, \quad (3)$$

322 where  $\rho_a = 1.1 \text{ kg m}^{-3}$  is the density of air.

323 In order to investigate the dependence of the snow redistribution on the strength  
 324 of the fluid-threshold in the further course of the work, we introduce the factor  $\alpha$ , which  
 325 allows us to scale the fluid threshold:

$$\tau_{th}^* = \alpha \cdot \tau_{th}. \quad (4)$$

326 For the base setup, we kept  $\alpha$  at 1.0, which we called reference setup (R). However,  
 327 we also performed simulations with  $\alpha = 3.0$ , which led to changes in the mass balance  
 328 and density, which we would therefore like to present in addition. In the following, we  
 329 call these simulations comparison scenario (C).

#### 330 **2.4.6 Mass balance treatment**

331 The ALPINE3D drifting snow routine (Doorschot & Lehning, 2002) computes for  
 332 each time step a global steady state condition for the location of snow mass in the air.  
 333 The location and magnitude of eroded mass that is entrained into the air (and deposits  
 334 somewhere else) depends on the fluid threshold that is explained in section 2.4.5. Hence,  
 335 at each pixel in the domain, a SNOWPACK simulation returns the amount of snow eroded/deposited  
 336 at each time step to the ALPINE3D model kernel. The drifting snow routine can only  
 337 erode one snow layer at a SNOWPACK model timestep, which is 15 min. in this study.  
 338 As the computed amount of mass in the air depends on the snow properties of the up-  
 339 permost snow layer, deeper layers can exhibit a stronger bond and higher density, reduc-  
 340 ing the erosion. In this approach, at a certain cell, the computed eroded mass may be  
 341 greater than either the actual available mass of the surface layer. It might also be the  
 342 case that the total mass on the ground is less than the eroded mass computed by the  
 343 drifting snow routine. In both cases, the suspended (and later deposited) mass is greater  
 344 than the total snow mass actually available for erosion. In addition, since precipitation  
 345 is consumed in the drifting snow routine and snow is allowed to remain in suspension,  
 346 snow might never be deposited and the deposition rate might be lower than the precip-  
 347 itation rate. In order to close the mass balance, the following approach was implemented  
 348 in the model:

- 349 1. For each pixel and time step, the erosion mass returned by the drifting module  
350 is limited to the mass of the uppermost layer.
- 351 2. The global mass balance, i.e. the deposition plus the precipitation minus the cor-  
352 rected erosion is computed.
- 353 3. If the mass balance is positive, the deposition is linearly decreased for all pixels  
354 in order to obtain a zero value for the mass balance. If the mass balance is neg-  
355 ative, the deposition is linearly increased for all pixels in order to obtain a zero  
356 value for the mass balance.

357 At deposition time, the density of deposited new snow is set to the deposited snow  
358 density (Section 2.4.4).

#### 359 *2.4.7 Snow cover measurements*

360 SnowMicroPen (SMP) resistance force measurements (Schneebeli & Johnson, 1998)  
361 conducted at the same four positions along the Northern transect at around 12 UTC on  
362 16 Jan, 30 Jan and 6 Feb (Fig. 2). At each location and on each day, 5 measurements  
363 were conducted. Out of the collected force profiles, densities were computed as by King  
364 et al. (2020) Wagner et al. (2022) and the 5 density profiles were averaged after align-  
365 ing with the snow surface. Out of the four positions, only the profile of SMP3 was cov-  
366 ered by the model domain (Fig. 2b). The surface density determined in this way will be  
367 used for comparison with the model.

368 In addition, a Magnaprobe (Sturm & Holmgren, 2018) was used to measure snow  
369 depths along the Northern Transect on a weekly basis, ice and weather conditions per-  
370 mitting. The methodology of the measurements and the data set are described in de-  
371 tail by Itkin et al. (2021). Furthermore, we derived snow depths from the SMP measure-  
372 ments. We use the snow depth data from both instruments to compare the differences  
373 between the individual days with those of the model.

#### 374 *2.4.8 Initial snow cover*

375 To initialize the ALPINE3D snow cover, we first created a snow profile for SNOW-  
376 PACK based on an horizontally averaged SMP density profile measured on 16 Jan from  
377 all the SMP1 – SMP4 locations, on the northern transect (Fig. 2b). The 20 single pro-  
378 files were first aligned along the surface and made an horizontally averaged profile. As  
379 the middle part of the profile was mostly vertically constant in terms of density but not  
380 the lowest part (due to temperature gradient metamorphism) and the most upper part  
381 (due to wind compaction), and in order to get the best estimate for temperature and den-  
382 sity, we extracted the upper 11 cm and the lower 11 cm of this average profile and cre-  
383 ated an initial SNOWPACK composite profile out of the extracted upper and lower part.  
384 The average density of the initial profile is  $285 \text{ kg m}^{-3}$ . With this profile, we made a sin-  
385 gular (1D) SNOWPACK spin-up run until 26 Jan 1000 UTC forced by the meteorologi-  
386 cal measurements. The density state on 26 Jan 1000 UTC of the profile is shown in Fig. 4.  
387 The increase of snow height between 16 and 26 Jan is only 1 cm, which corresponds to  
388 1.3 mm of SWE. The profile properties are rather constant with height, however with  
389 a slightly decreased density toward the bottom due to depth hoar formation and a wind  
390 slab at the top. The profile mostly consists out of depth hoar in the lower part (dark blue  
391 in Fig. 4), faceted grains (light blue) in the upper part, a layer of rounded grains (ma-  
392 genta) in the upper part as wind slab. This profile out of the spin-up was then distributed  
393 uniformly over the ALPINE3D domain and is used as initial state on 26 Jan 1000 UTC.  
394 The total height of the initial profile (23 cm) is approximately consistent with the av-  
395 erage snow depth of the northern transect measured with the Magnaprobe on 30 Jan (26.7 cm).

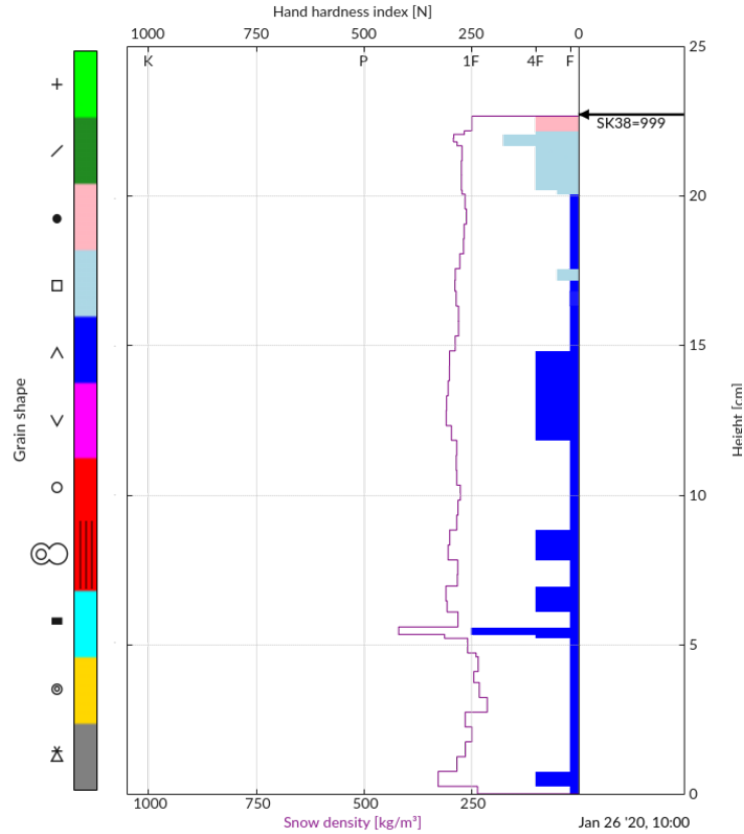


**Figure 4.** The initial profile after spin-up at 26 Jan 1000 UTC, which was distributed over the domain as ALPINE3D initial snow cover state at each grid cell. The colors indicate the grain shapes as classified by Fierz et al. (2008), where the legend on the left describes the relationship between the shown colors and grain shape symbol.

396

#### 2.4.9 1D SNOWPACK simulations

397

398

399

400

401

402

In order to investigate whether the computationally expensive ALPINE3D setup offers advantages over a computationally very cost-effective 1D SNOWPACK simulation with regard to the calculation of the surface density, we set up 2 SNOWPACK simulations for comparison, which we ran from 16 Jan based on the initial profile (Section 2.4.8). Both simulations were set up with the same settings as R and C - only 1-dimensional - therefore they are called SP\_R and SP\_C in the following.

403

### 3 Results and Discussion

404

#### 3.1 Drifting snow mass fluxes

405

406

407

408

409

410

411

412

In the following, we evaluate the model in terms of snow transport SPC measurements, which took place at the same flux tower as the wind measurements used to drive the model. To make a comparison possible, we defined a normalized mass flux for the lower SPC at 0.1 m above the surface simply as a ratio of instantaneously measured mass flux relative to the maximum measured over the whole investigation period. For the model, we used the spatial average of the instantaneous absolute values at each grid cell with respect to deposited and eroded saltation mass ( $\text{kg m}^{-2}$ ). As for the SPC, we normalized the averaged absolute saltating mass. By doing so, we are able to compare the tim-

413 ing of snow transport as well as the relative magnitudes with the measurements. The  
 414 normalized mass flux, measured at the lower SPC at 0.1 m above the surface, is very well  
 415 represented by the normalized mass flux in the reference model setup (Fig. 5c,d). The  
 416 frequency distributions of measured mass flux at the 0.1 m SPC versus the modeled mass  
 417 flux plotted as a wind rose (Fig. 6) indicate well simulated mass flux with respect to wind  
 418 direction, as well. Note that the ratio in the NNW sector is under-represented in the model.  
 419 The reason is probably that in reality the SPC was wind-shadowed by relatively high  
 420 ridges in the NNW sector and the mentioned installed hut, leading to under-sampling  
 421 of drifting snow particles for this wind direction.

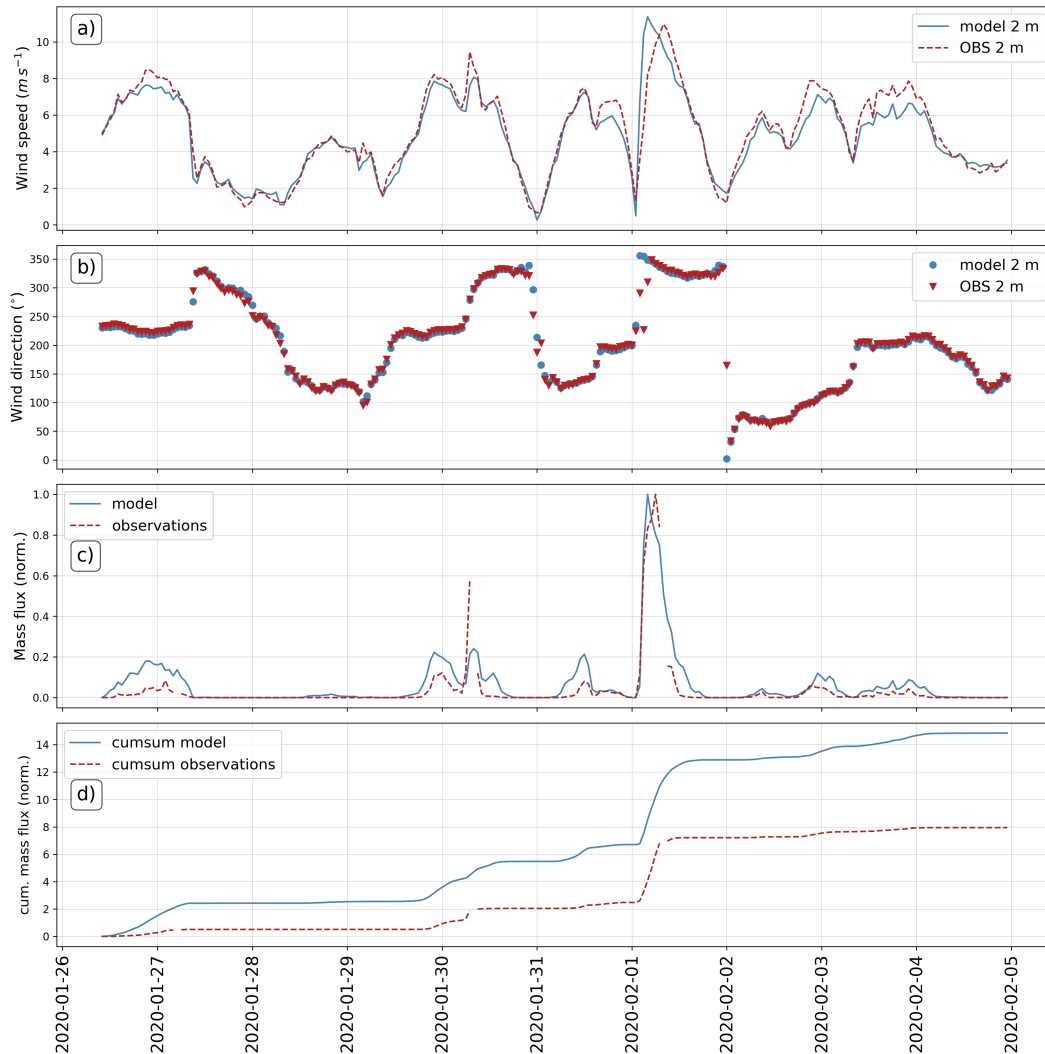


**Figure 5.** a) 2-meter tower-observed wind speed (1 h avg) versus horizontally averaged 2-meter modeled wind speed from OpenFOAM. b) Same as for a), but for wind direction, c) modeled (R) and measured normalized drifting and blowing snow mass flux over time. d) modeled (R) and measured cumulative normalized drifting snow mass flux over time.

422 However, also note that average (domain-wide) modeled mass flux is compared with  
 423 point measurements that were measured a few hundreds of meters away from the area  
 424 that is represented in the model. In addition, the SPC was partially wind-shadowed by

425 ridges in its Western and North-western direction, making accurate absolute compar-  
 426 isons very difficult.

427 Nevertheless, the results show that the model can be used to determine the tim-  
 428 ing of drifting snow events and relative mass flux with very high accuracy ( $r = 0.92$ ).

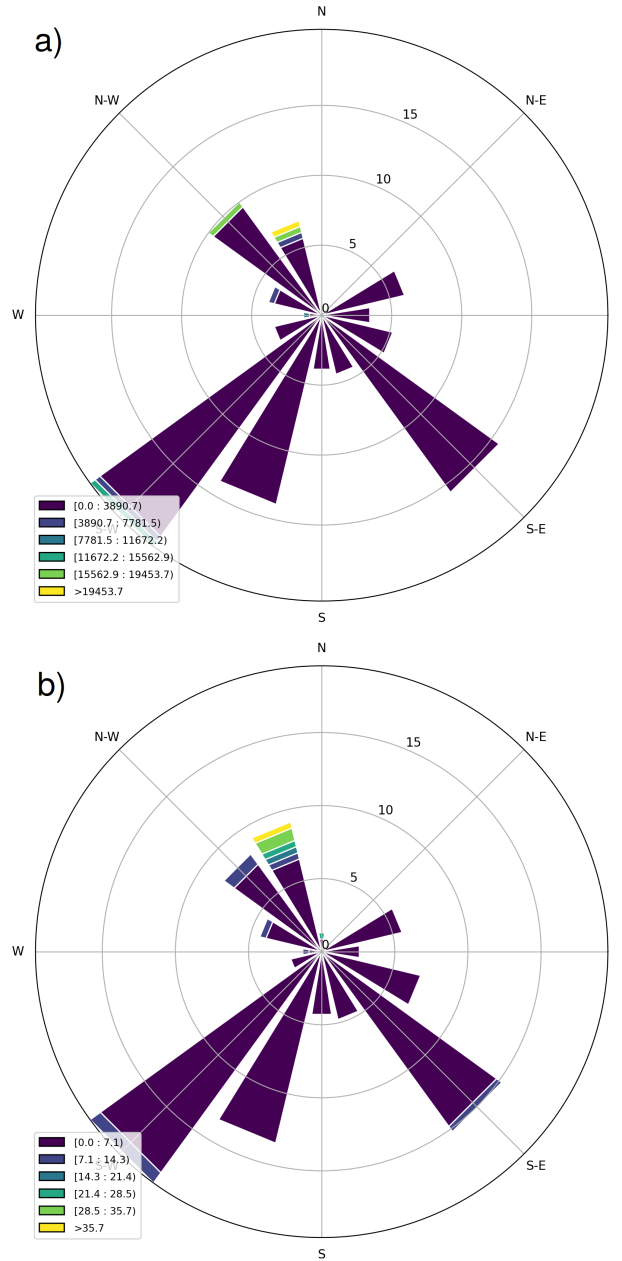


**Figure 6.** a) Wind rose for the measured mass flux with the lower SPC (0.1 m). b) Wind rose for the modeled spatially averaged absolute saltation deposited and eroded flux.

### 429 *3.1.1 Potential uncertainties regarding the drift threshold*

430 It is noteworthy that  $A$  and  $B$  in Equation 2 are empirically determined. We choose  
 431 the values as used by Clifton et al. (2006) ( $A = 0.023$  and  $B = 0.0035$ ). However Keenan

et al. (2021), for instance used the parameters  $A = 0.02$  and  $B = 0.0015$  as it was recently implemented in SNOWPACK. In our case, we found a tendency of the model to compute the initiation of saltation at too low wind speeds relative to the measured mass flux, extending the drifting snow time periods in the model over the measured ones. Hence, as increased  $A$  and  $B$  parameters increase the fluid threshold, we chose to use the older values.

Note, that the surface snow density - hence the used deposited snow density parameterization (Equation 1) is indirectly affecting the fluid threshold, and therefore the re-distribution. The coordination number  $N_3$  - a factor in the second term of the fluid threshold equation (Equation 2) - fitted by Lehning et al. (2002) and used in the recent SNOWPACK version in the following form, is directly dependent on the bulk density of snow  $\rho_s$ :

$$N_3 = 1.42 - 7.56 \cdot 10^{-5} \rho_s + 5.15 \cdot 10^{-5} \rho_s^2 - 1.73 \cdot 10^{-7} \rho_s^3 + 1.81 \cdot 10^{-10} \rho_s^4. \quad (5)$$

Hence, the adjusted deposited snow density is affecting directly  $N_3$  and hence indirectly affecting  $u^*_{th}$  (Equation 3), leading to an increased  $u^*_{th}$  with increasing density.

Since only wind measurements took place outside the model domain, we were only able to fit wind speeds in the model as domain-average to the measurements from a station slightly outside the model domain. Thus, the model wind profile may not fit the measurements well in every case. Furthermore, the values for  $A$ ,  $B$  and  $\sigma$  were found empirically, either in a wind tunnel or from experiments in the Alps. In fact, general wind and environmental wind conditions are quite different to conditions in the Alps and most likely, wind tunnels as well. In addition, there are several other factors, like the particle entrainment coefficient, where the value currently used in SNOWPACK has been found empirically (Groot Zwaafink et al., 2014) at it is likely that the environmental conditions during that study do not resemble those of our study. Hence, several other empirical fitting parameters are not necessarily correct for snow on sea ice, as well.

### 3.2 General mass balance

In this section we want to examine the following points, related exclusively to the parameter of the snow depth difference:

1. Investigate basic spatial statistics of the modeled snow height differences and how it compares to the measurements.
2. Having a statistical view on the spatio-temporal change of snow distribution in the model.
3. Conduct spatial correlations of snow height differences compared to model measurements and compared to previous studies on sea ice (Sturm et al., 2002; Liston et al., 2018).
4. Do a qualitative evaluation of spatial differences model versus observation.
5. Investigate time series averages of various parameters and compare them with 1-D SNOWPACK simulations

#### 3.2.1 Frequency distributions of snow height differences

The frequency distribution of the spatial snow depth difference between the two laser scans can well be described by a Cauchy distribution (Fig. 7a).

In order to evaluate the spatial snow distribution of the various model runs quantitatively with time, first we generated maps of 2-dimensional snow depth differences  $\Delta HS_{i,j,t-t_0}$  for both, model output and TLS:

$$\Delta HS_{i,j,t-t_0} = HS_{i,j}(t) - HS_{i,j}(t = 0). \quad (6)$$

467 where  $HS_{i,j}(t)$  is the total snow height at each point of the grid at time  $t$ , with  $i, j$  be-  
 468 ing the horizontal indices for the grid points in  $x$  and  $y$  direction, respectively, and  $HS_{i,j}(t =$   
 469  $0)$  is the total snow height at each point of the grid at time  $t = 0$ .

470 In Fig. 7a we see that the distribution is almost symmetrical along the  $y$ -axis, how-  
 471 ever, also slightly skewed. The location on the  $x$ -axis  $x_0$  also indicates that the peak is  
 472 slightly shifted toward negative values.

473 The distribution is generally well reproduced by the model (Fig. 7a). However, the  
 474 modeled distribution is rather described by a Gaussian than a Cauchy distribution as  
 475 observed. Especially, it is noticeable that the negative range of the distribution is less  
 476 pronounced for more negative values, which indicates less area of erosion for higher depths  
 477 in the model.

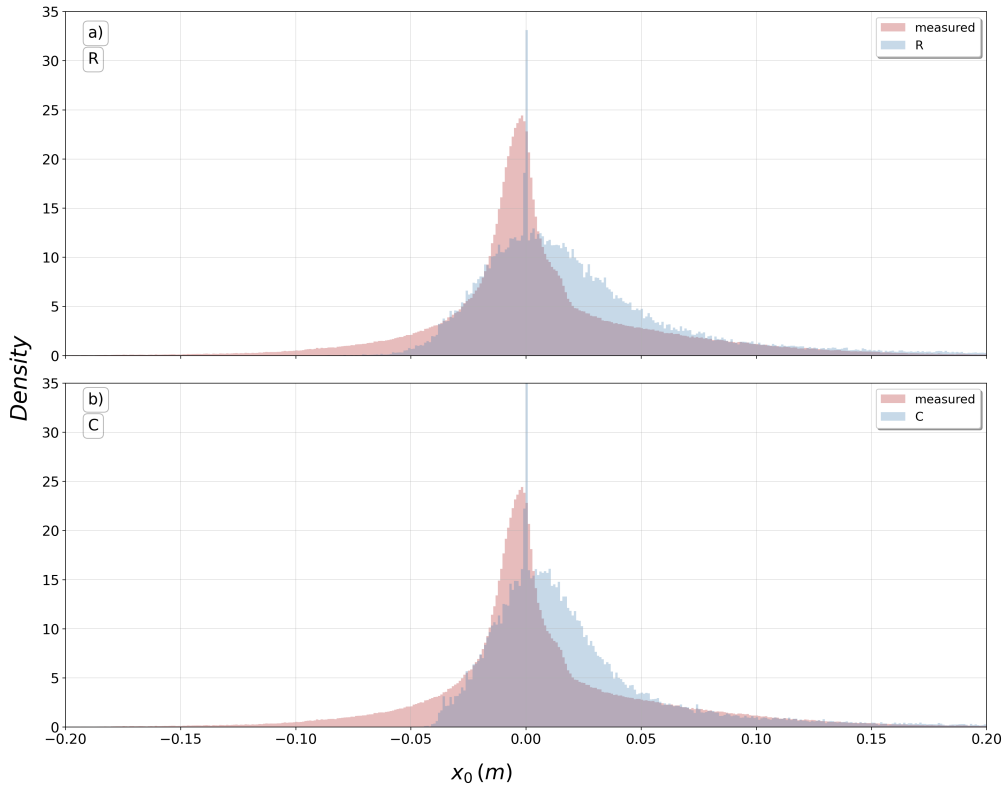


**Figure 7.** Frequency distributions for modeled snow depth differences between first and last hour of the model output and TLS measured difference. a) shows the reference, b) the C scenario

478 One reason for this could be the neglect of the spatial variability of the snowpack  
 479 in the initialization of our model. Areas where snow drifts were deposited shortly be-  
 480 fore 25 Jan will be relatively easier to erode than snow that has deposited earlier and  
 481 sintered for a longer time. The negative tail in the observations could be the erosion of  
 482 these recent drifts. Because the model uses uniform snow properties, it does not resolve  
 483 these recent drifts and hence misses the negative tail. Hence, bringing the distribution  
 484 from the model output in closer agreement with observations is very difficult, if not im-  
 485 possible, as we not only had to guess the initial distribution of snow mass but also the  
 486 distribution of the snow properties based on point measurements.

487 Compared to the R scenario, the C scenario with  $\tau_{th}^* = 3.0$  (Fig. 7b) shows a less  
 488 compressed distribution, but also with less pronounced legs to the sides. For us, this is  
 489 an indicator that less redistribution has taken place in the C scenario due to the higher  
 490 fluid threshold.

491 **3.2.2 Statistical view on the spatio-temporal change of snow distribu-**  
 492 **tion**

493 The model enables the detailed study of events within the time-span of two laser-  
 494 scans. To examine the temporal evolution of the spatial distribution in detail statisti-  
 495 cally, we consider histogram time series for the modeled snow depth difference of the ref-  
 496 erence scenario (Fig. 8a) versus the comparison scenario (Fig. 8b) based on Equation 6.  
 497 Although we detected 4 main drifting snow events within the investigation period initial-  
 498 ly by means of the measurements (Fig. 1), the histogram time series of the reference  
 499 (Fig. 8a) shows that the snow cover in the simulation was affected by re-distribution most  
 500 of the time. However, simulation C shows much less dynamics (Fig. 8b), and the distinct  
 501 events for this setup can mainly be reduced to the 4 main events as detected solely with  
 502 the measurements. This raises the question which scenario is more realistic - relative mass  
 503 flux comparisons (Fig. 5c) suggest that the mass flux for the reference run was too high.  
 504 From this we conclude that the redistribution in the C scenario is probably more real-  
 505 istic. A detailed verification over time does require a significantly higher frequency of  
 506 measurements of the snow depth difference.

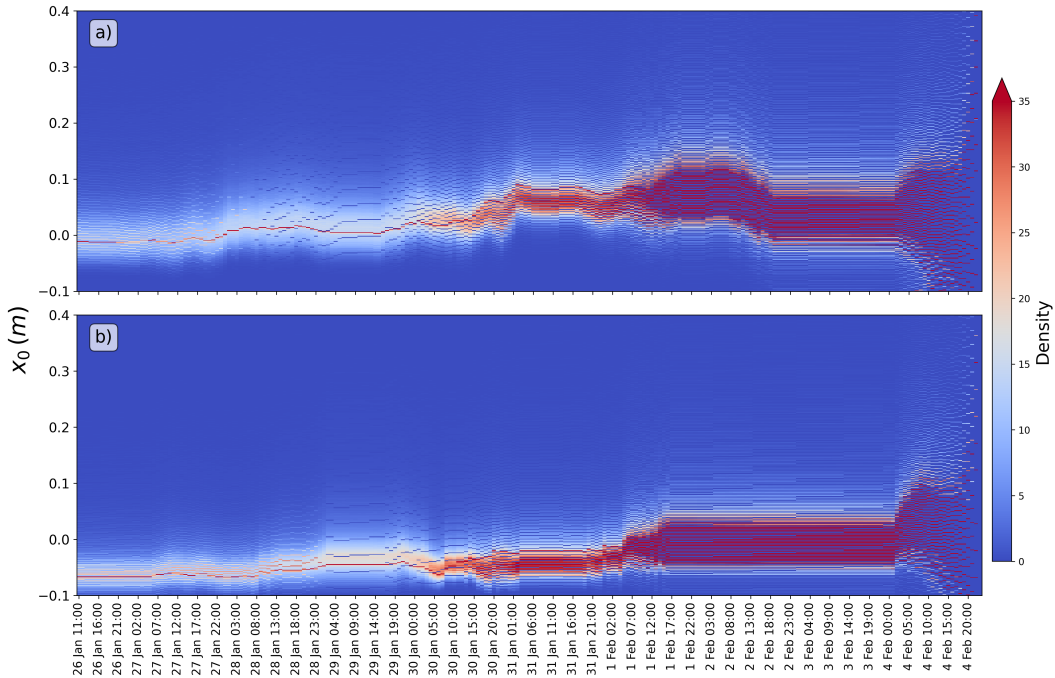


**Figure 8.** 2-D time series of the frequency distributions as shown in Fig. 7a, for a) R scenario and b) for the C scenario. Each time step shows one histogram for the difference of snow depth at the time with respect to the snow depth at  $t = 0$ . The color indicates the density.

### 3.2.3 Spatial correlation

To evaluate the spatial correlation of snow depth differences, we can look at semi-variograms, which have been generated using the Python SciKit-GStat library (Mälicke, 2022). To estimate the semi-variance, we used a Matheron estimator function (Matheron, 1963):

$$\gamma(h) = \frac{1}{2N(h)} \sum_{i=1}^{N(h)} (x(P_i) - x(P_{i+h})), \quad (7)$$

where  $N(h)$  is the number of point pairs for the lag distance  $h$  (in meter), and  $x$  (in meter) is the observed value at its location  $P$ . Hence, semi-variograms describe the spatial correlation of point pairs as a function of their distances from each other. The computed semi-variogram for the snow height difference of the observation and the R scenario is shown in Fig. 9a. The measured difference has a smoother transition from highest correlation towards least (constant) correlation, which is reached at a range of approximately 6 m distance. The transition towards least correlation in the model is less smooth, though also reached at approximately 6 m distance. The correlation decrease occurs fast in the model, with a quick decrease from 0 to 2 m distance, and less decrease from 2 m onward. The differences between reference (Fig. 9a) and comparison scenario (Fig. 9b) are not large, although a generally larger positive deviation of the semi-variance is observed for the comparison scenario for the whole lag distance.

We expect a less smooth transition from high towards low (steady) correlation to be a result of less long-stretched deposition and erosion patterns in the model output. The reason could be that our grid is static and does not dynamically adapt to the snow surface over time. In order to get the model to produce dunes, an adaptive mesh that accounts for newly deposited or eroded snow at each time step, would be required. This is not implemented in the current setup.

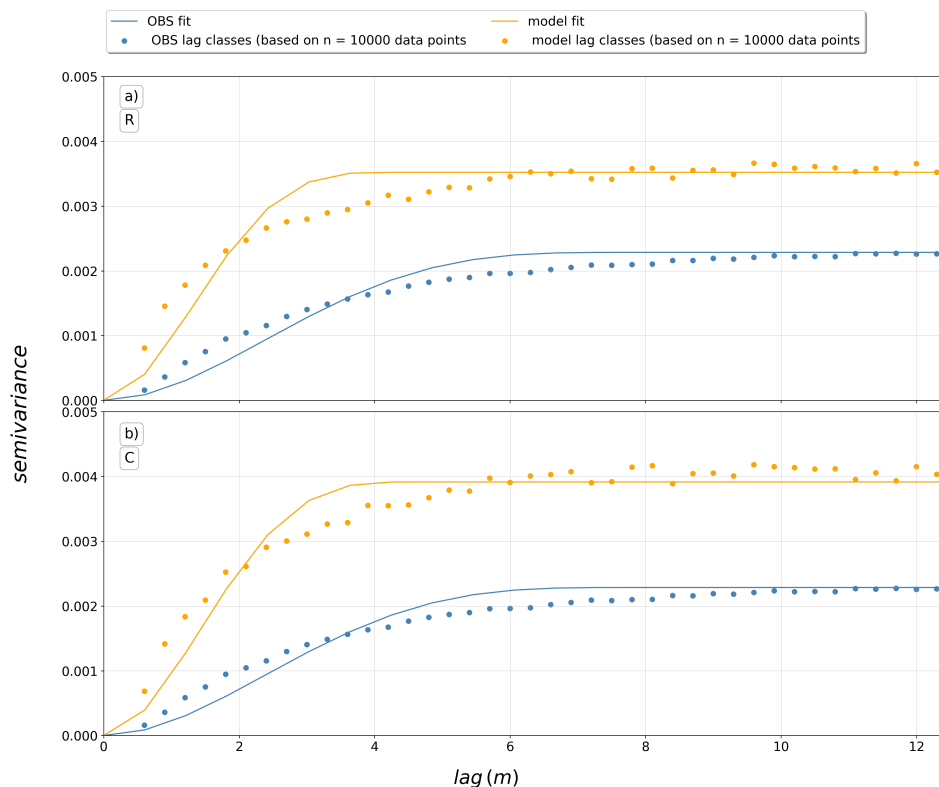


**Figure 9.** Semi-variance for modeled snow depth differences between first and last hour of the model output and TLS measured difference for a) the reference scenario R, b) scenario C.

526 It is noteworthy that, in a qualitative comparison, ranges of semi-variograms for  
 527 absolute snow depth distributions over Arctic sea ice compares with other studies on Arctic  
 528 sea ice (Sturm et al., 2002; Liston et al., 2018). Liston et al. (2018), for example, ex-  
 529 amined semi-variograms based on snow depth measurements along various transects mea-  
 530 sured during the Norwegian Young Sea Ice Experiment (N-ICE2015) field campaign and  
 531 a snow cover model which models the snow height spatially for the respective same area.  
 532 For both the measurements and the model, a range of almost 6 m was observed, simi-  
 533 lar to our results. Sturm et al. (2002), on the other hand, examined semi-variograms based  
 534 on snow depth measurements along various transects during the Surface Heat Budget  
 535 of the Arctic Ocean (SHEBA) campaign of the years 1997-1998. Here, mostly larger ranges  
 536 between 13 and 30 m were found, but most of them in the lower end of this range. Since  
 537 we compare snow depth difference in our case with absolute snow depth in the other two  
 538 studies, the absolute values of the semi-variance are logically of different magnitudes. How-  
 539 ever, it is clear that during our measurements, and the measurements during SHEBA,  
 540 fundamentally different snow conditions prevailed. Webster et al. (2014), for example,  
 541 has calculated that between the years 1950 and 2014 the mean snow depth on Arctic sea  
 542 ice decreased by 2.9 cm per year. If we now look at the relatively large mean snow depths  
 543 at the end of the winter season during SHEBA (33.7 cm) and extrapolate over the value  
 544 would arrive at 27.4 cm for MOSAiC, which is not far from the measured value from Wagner  
 545 et al. (2022) (24.9 cm). In addition, Merkouriadi et al. (2017) reports strongly different  
 546 proportions of depth hoar or faceted grains and wind slab in the snowpack for N-ICE2015  
 547 compared to SHEBA and Sturm et al. (2002) reported consistently low temperatures that  
 548 favored the development of depth hoar, while both Merkouriadi et al. (2017) reported  
 549 warm air intrusions in winter, as did Shupe et al. (2022) for MOSAiC. Overall, then, we

550 must assume that snow conditions differed greatly, particularly between SHEBA and N-  
 551 ICE2015 or MOSAiC.

552 Nevertheless, the strong similarity of the values between (Liston et al., 2018) and  
 553 our study suggest that snow conditions were more similar between N-ICE2015 and MO-  
 554 SAiC, especially in terms of spatial snow distribution.

### 555 3.2.4 Qualitative evaluation of spatial differences

556 Spatial correlations allow for quantitative comparisons, however, they do not re-  
 557 veal all properties of spatial variation. Therefore, qualitative comparisons with respect  
 558 to the localization of drifting snow patterns are made in the following section.

559 Absolute snow height outputs for the R and the C model are shown in Fig. 10a and  
 560 Fig. 10b, respectively. Surface densities (discussed later) are shown in Fig. 10c,d. Over-  
 561 all, higher maximum snow heights can be observed for the C scenario (Fig. 10b). We as-  
 562 sume that this is due to initially precipitated snow (precipitated under conditions when  
 563 snowfall and wind prevail at the same time) that is less prone to erosion and therefore  
 564 removal.

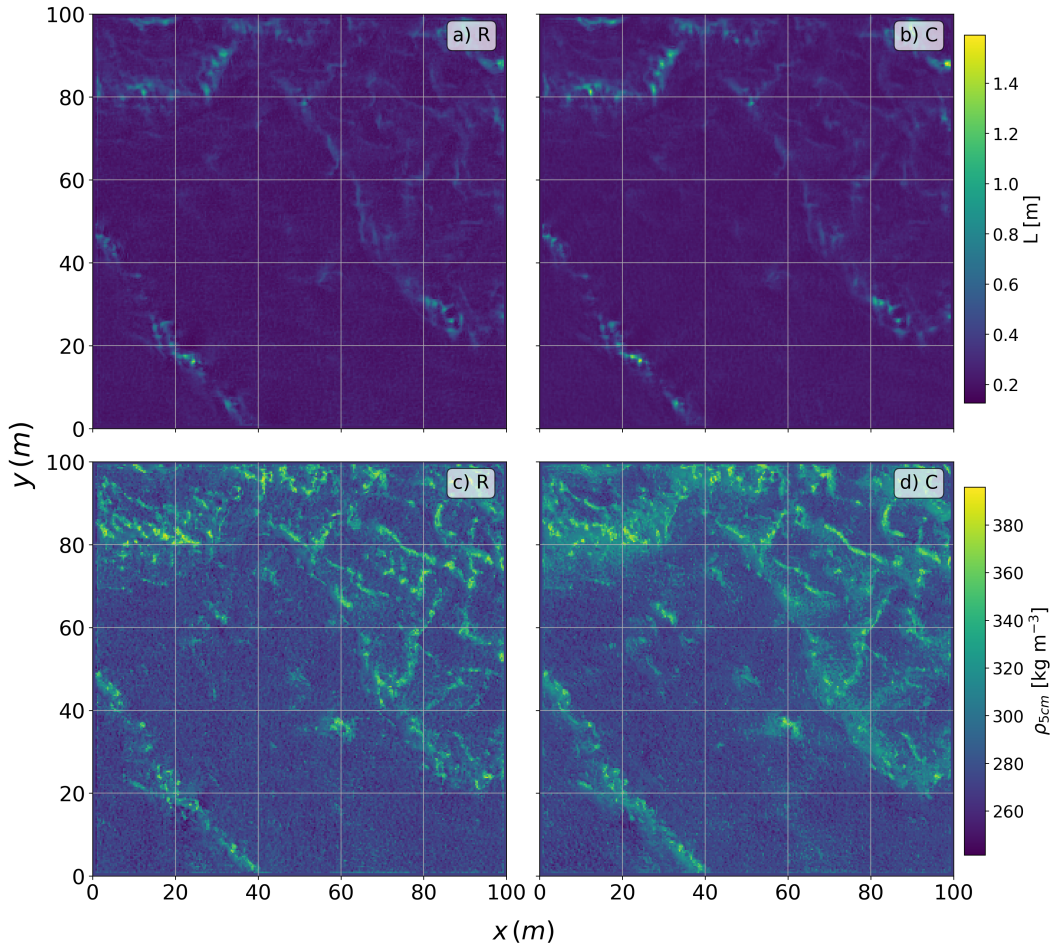


**Figure 10.** a) modeled (R) absolute snow height, b) modeled (C) snow height, c) modeled (R) surface density  $\bar{\rho}_{5cm}$  and d) modeled (C) surface density  $\bar{\rho}_{5cm}$ .

565 The comparison of the spatial distribution of absolute snow depth differences be-  
566 tween model reference and TLS measurements is shown in Fig. 11a,b. Purely visually,  
567 the spatial distribution does not appear to be particularly well reproduced by the model.  
568 In addition, as already mentioned, dunes in flat areas are almost not reproduced. How-  
569 ever, there are locally good model results, and examples for this are marked in orange  
570 circles. In addition, as in the TLS observations, snow mass is preferably deposited along  
571 the distinct ridge in the lower left corner of the domain - although the specific locations  
572 and scales of the deposited mass are different from those that are observed. Erosion does  
573 occur in the model as well, although at a much lower magnitude than observed, espe-  
574 cially around the distinct ridge. Correlations and anti-correlations between model and  
575 TLS can also be observed, which depend primarily on the topography. Besides the ridge  
576 at the bottom left of the domain, stronger structures at the top left are visible in both  
577 the model and the TLS. The same is true for an edge that runs from about  $x = 40$ ,  $y$   
578  $= 90$  to  $x = 100$ ,  $y = 20$ . However, this edge is clearly of an anti-correlative nature. The  
579 reasons for this are currently unknown. Another location where erosion and deposition  
580 is well reproduced in the model is cross section S1 (discussed in detail in Section 3.4.  
581 We further will look into detail at cross section 2 and cross section 3. In order to see if  
582 the total accumulated snow is affecting the patterns visually, we normalized the abso-  
583 lute distributions for model and TLS respectively (Fig. 11c,d), i.e. the respective differ-  
584 ence values at each index point were divided by the highest difference value per domain.  
585 In this representation, the differences between the model and TLS are no longer quite  
586 so drastic.

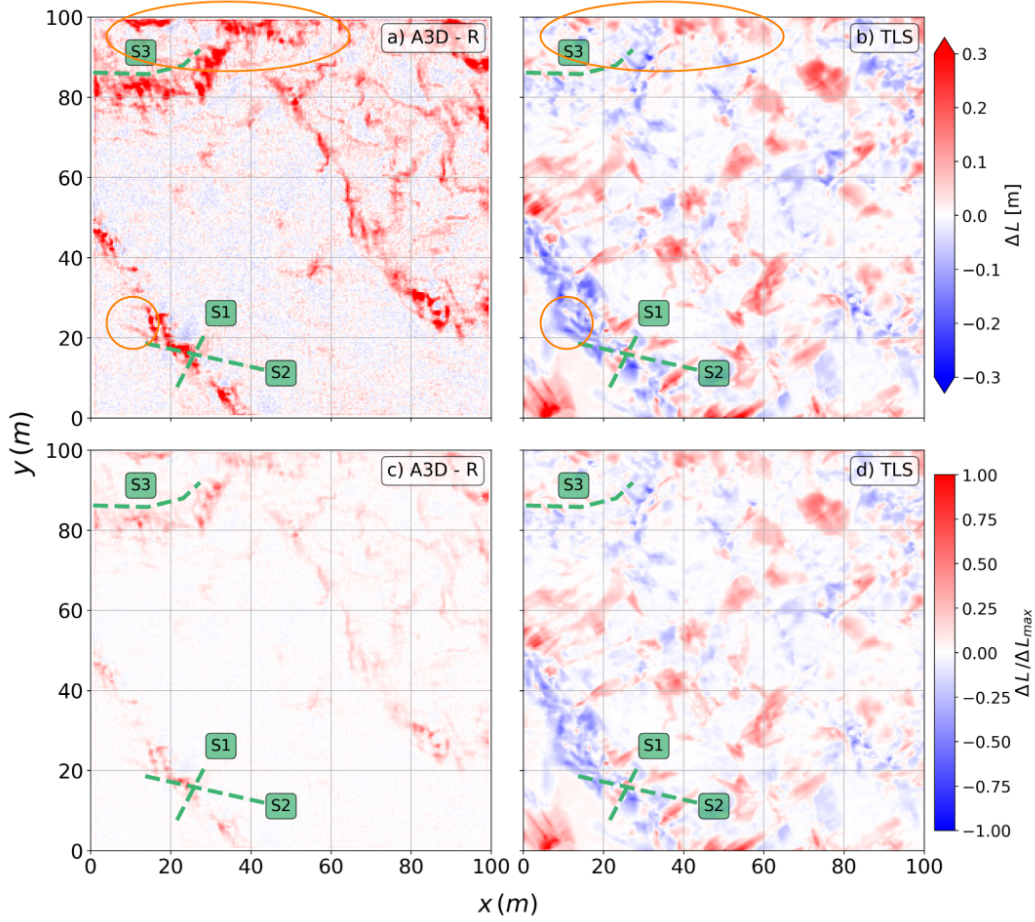


**Figure 11.** a) modeled snow depth difference between 26 Jan and 4 Feb for the R model run, b) is the measured snow depth difference via TLS between 26 Jan and 4 Feb, c) shows the modeled normalized snow depth difference for the R model run and d) shows the measured normalized snow depth difference from the TLS.

587  
588

### 3.2.5 Time series averages and comparisons with 1-D SNOWPACK simulations

589  
590  
591  
592  
593  
594  
595  
596  
597  
598  
599  
600  
601

For a more detailed view of individual domain-averaged model parameters, we look at Fig. 12. Here, the individual events are more clearly visible for both, the reference and C scenario (Fig. 12). As expected, the C scenario ( $\tau_{th}^* = 3.0$ ) does most of the time produce lower snow transport rates, but partially even computes higher transport rates in comparison. This is valid for a short time span on the 30 Jan and on 1 Feb. Reasons for this rather uncommon behaviour still need to be investigated. Averaged snow height differences of the ALPINE3D C and R scenarios and their standard deviations, as well as two 1-D SNOWPACK simulation scenarios are shown in Fig. 12d and Tab. 1, compared against TLS-measured snow height averaged difference, Northern Transect Magnaprobe snow height averaged difference and SMP-derived snow height differences. For the SNOWPACK simulations, all parameters in the setup were kept the same as in ALPINE3D R and C, the only difference is that there is no snow transport available like in the 3D drift simulations.

602 The TLS-based difference on 4 Feb for the model domain only gives +0.007 m, while  
603 the Northern transect on 6 Feb gives +0.042 m. However, note that when considering  
604 a larger area, the TLS increase is approximately +0.014 m. If we only choose the sec-  
605 tion of the transect that is covered by the domain (Fig. 2b), the transect-based increase  
606 is +0.031 m. Hence, the modeled averaged A3D snow height difference by the end of the  
607 simulation period lays between the lowest and highest average values of measurements  
608 available. The intermediate transect-based measurement on 30 Jan shows an increase  
609 of +0.012 m (short section: +0.009 m).

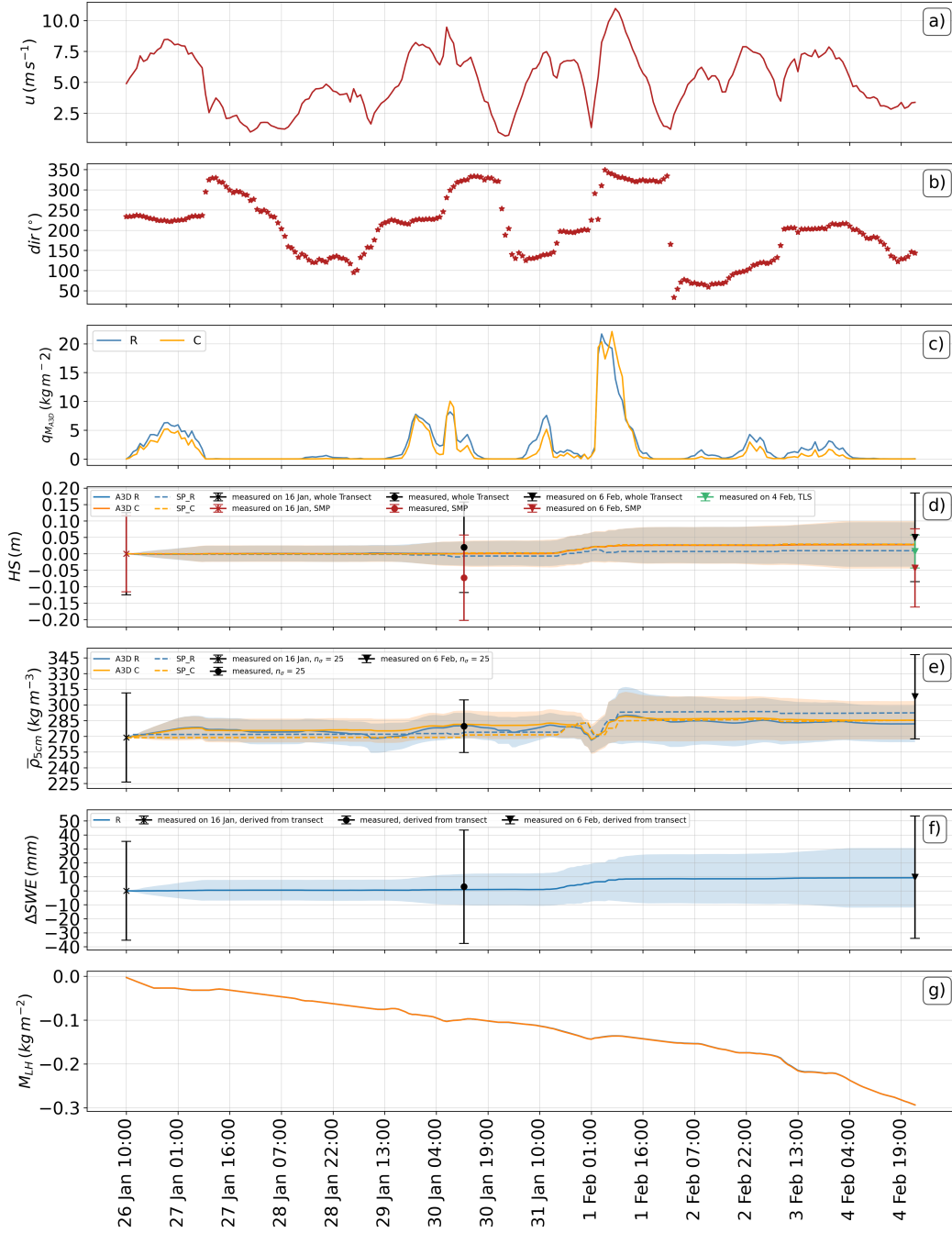


**Figure 12.** Time series (1h avg) of a) horizontally averaged wind speed (2 m), b) horizontally averaged wind direction (2 m), c) average of absolute deposited and eroded saltation mass per grid cell, d) spatially averaged modeled snow depth and its standard deviation, e) spatially averaged  $\bar{\rho}_{5cm}$  modeled snow density, f) cumulative precipitation sum retrieved from KAZR and spatially averaged cumulative  $\Delta SWE$ , g) cumulative sublimated or deposited ice mass (negative = vapor deposition).

610 One should consider the following measurement uncertainties in this regard: First,  
 611 note that the low TLS difference is in part due to erosion of snow drifts along the first-

612 year ridge (in the lower left, Fig. 10). However, the transect does not include this ridge,  
 613 so it misses this erosion. Additionally, it might be possible that the characteristic flut-  
 614 ing and scalloping erosional patterns of sastrugi (Filhol & Sturm, 2015) and the steep  
 615 snow topography of drifts around ridges (e.g., Fig. 11) cause the Magnaprobe measure-  
 616 ments to be biased high due to the 25 cm diameter Magnaprobe basket getting propped  
 617 up on a local high point. In other words, each Magnaprobe observation measures approx-  
 618 imately the maximum snow thickness within the basket footprint. However, there are  
 619 currently no concrete evaluations of this in the literature. Detailed methodological com-  
 620 parison of transect and TLS measurements is beyond the scope of this manuscript and  
 621 will be investigated in future work.

622 The standard deviation with time serves as an approximate indicator of snow re-  
 623 distribution over time, making the four drifting snow events clearly visible. However, there  
 624 is no clear difference between R and C. Based on other simulation results, we can say  
 625 that if there is a more significant difference in the factors  $\alpha$  for  $\tau_{th}^*$  used, a significant dif-  
 626 ference is also visible in the standard deviation: with a higher standard deviation for lower  
 627  $\tau_{th}^*$  values. Fig. 2e shows the same as in Fig. 12d but for the average surface density of  
 628 the first 5 cm of the snowpack ( $\bar{\rho}_{5cm}$ ). A consequence of the decreased snow transport  
 629 in the C scenario is, that the averaged density is increased over the R scenario. Possi-  
 630 ble reasons for this are discussed in detail in the next section. Fig. 2f shows the modeled  
 631 averaged snow-water equivalent (SWE) difference over time, compared with northern transect-  
 632 derived SWE as reported by Wagner et al. (2022). The mean increase in SWE in the model  
 633 here is equivalent to the precipitation sum for the same period, which was used as the  
 634 model input. This is the retrieval based on the Ka-band cloud radar as used in Wagner  
 635 et al. (2022). It is noteworthy, that although the model shows a slight difference rela-  
 636 tive to the intermediate measurement, it fits exactly the estimated SWE increase of 9 mm  
 637 (based on the whole transect). Fig. 12h shows the modeled surface sublimation with time.  
 638 Negative values corresponds with vapor deposition. Based on this time series, we can rule  
 639 out the possibility that 1) sublimation occurred at all and 2) that water vapor deposi-  
 640 tion occurred in relevant amounts that significantly affected the surface mass balance  
 641 in a positive way.

### 642 3.3 Surface snow density

643 In the following, we compare the modeled snow densities - with a focus on the sur-  
 644 face density - with measurements. We compare the surface density rather than the den-  
 645 sity of the total snowpack because, first, it is relevant to the timing, location and mag-  
 646 nitude of the mass of erosion as a function of wind speed and fluid threshold, as described  
 647 in Section 2.4.5 and Section 2.4.6. Second, the upper centimeters of the snowpack on sea  
 648 ice often consist of wind slab (Sturm et al., 2002; Merkouriadi et al., 2017), which re-  
 649 duces the horizontal variability of density when averaging vertically. Since we only have  
 650 20 individual measurements available with the SMP per measurement day (5 per pit lo-  
 651 cation), we therefore have better comparability with the model using this approach.

#### 652 3.3.1 Measured snow density

653 Fig. 13 shows the horizontally averaged snow densities for the snowpack's top 5 cm  
 654 ( $\bar{\rho}_{5cm}$ ) based on Pit 1 – Pit 4 measured with the SMP (locations shown in Fig. 2), for  
 655 16 Jan, 30 Jan and 6 Feb.  $\bar{\rho}_{5cm}$  increases from 16 to 30 Jan and then further until 6 Feb.  
 656 For each day, seen from the surface, a rapid increase in density is observed as the snow  
 657 depth decreases downwards, followed by a slow decrease. This is probably due to wind  
 658 slab, a compaction of near-surface snow due to high wind speeds. The minimum is a lit-  
 659 tle bit under  $260 \text{ kg m}^{-3}$  on 16 Jan while the maximum is  $320 \text{ kg m}^{-3}$  on 6 Feb. Below  
 660 the wind slab we find more snow that has undergone temperature gradient metamorphism  
 661 and thus has a lower density. Similar observations of surface compaction during the MO-  
 662 SAiC expedition were described by Nandan et al. (2022), with even stronger expressions

Parameter	Observation			Model (avg $\pm$ $\sigma$ )			
	Device / Location	Date	OBS (avg $\pm$ $\sigma$ )	A3D R	A3D C	SP R	SP C
$\Delta HS$ (m)	MP Transect	16 Jan	0	-	-	(-0.004)	(-0.004)
	SMP	16 Jan					
	TLS	25 Jan	-		0		
	MP Transect	30 Jan	$0.02 \pm 0.138$	$0.001 \pm 0.037$	$0.0 \pm 0.039$	-0.01	0.003
	SMP	30 Jan	$-0.07 \pm 0.13$				
	TLS	4 Feb	$0.007 \pm 0.05$	$0.028 \pm 0.067$	$0.028 \pm 0.072$	0.006	0.03
	MP Transect	6 Feb	$0.05 \pm 0.135$			0.009	0.033
$\bar{\rho}_{5cm}$ ( $\text{kg m}^{-3}$ )		16 Jan	$268.9 \pm 42.5$	-	-	270.2	270.2
		26 Jan	-	268.6	268.6	268.6	268.6
	SMP	30 Jan	$279.7 \pm 25.2$	$280.1 \pm 12.3$	$281.4 \pm 13.1$	272.2	267.0
		4 Feb	-	$281.9 \pm 17.5$	$285.4 \pm 18.3$	292.6	272.4
		6 Feb	$307.8 \pm 40.3$	-	-	293.1	280.3

**Table 1.** Observed average snow height differences  $\Delta HS$  derived from the Magnaprobe (MP) measurements along the transect and by TLS differences with time as well as its respective standard deviations  $\sigma$ ; observed averaged density of the uppermost 5 cm of the snow cover ( $\bar{\rho}_{5cm}$ ) and its respective standard deviation over time, derived from the SMP along the transect, and the corresponding values from the modeled ALPINE3D (A3D) R and C scenarios and modeled SNOWPACK (SP) R and C scenarios. The bracketed negative values of the SP scenarios on Jan 16 represent the difference in the Jan 26 value minus the Jan 16 value for illustrative purposes, although the values themselves cannot be used for comparisons with the A3D model.

663 measured at a different location - a few hundred meters away a few weeks earlier, in November  
 664 as well as early December.

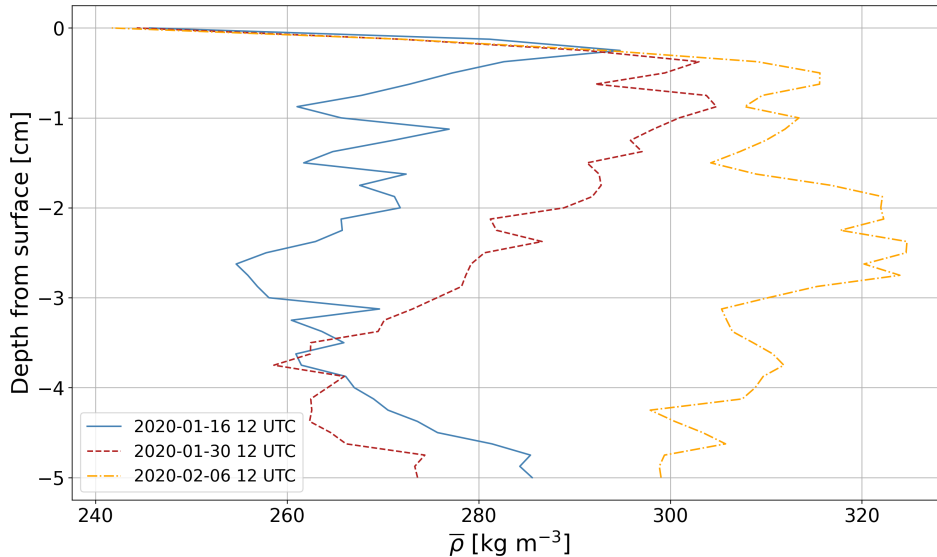


**Figure 13.** Horizontally averaged snow surface density profiles (5 cm depth) from snow pit 1-4 over time. Zero denotes the snow surface.

665 Fig. 14a confirms that for most of the pits,  $\bar{\rho}_{5cm}$  increases with time, and increases  
666 for all pits averaged from around  $270 \text{ kg m}^{-3}$  on 30 Jan to  $308 \text{ kg m}^{-3}$  on 6 Feb. In con-  
667 trast to the surface density, however, the total density (Fig. 14b) shows a somewhat dif-  
668 ferent picture: While for  $\bar{\rho}_{5cm}$ , the average density increases from 16 Jan to 30 Jan from  
669  $270 \text{ kg m}^{-3}$  by  $10 \text{ kg m}^{-3}$  to around  $280 \text{ kg m}^{-3}$  (Tab. 1), the average density for the whole  
670 profile decreases first slightly below  $280 \text{ kg m}^{-3}$  and then increases to little over  $290 \text{ kg m}^{-3}$ .  
671 Most interestingly, for the whole profile, the spread is strongly reduced on 30 Jan, com-  
672 pared to the spread before (16 Jan) and after (6 Feb). This is likely due to the fact that  
673 net erosion has occurred from the respective areas of the 4 snow pits: Mean snow depths  
674 derived from SMP measurements have decreased at each individual pit between 16 and  
675 30 Feb, namely -0.85 cm at Pit 1, -17.2 cm at Pit 2, -9.6 cm at Pit 3, and -2.0 cm at Pit  
676 4. This results in an average decrease of 7.4 cm. When we look at our initial snow pro-  
677 file on 16 Jan (Fig. 4) and the snow densities of the upper 5 cm (Fig. 14), it becomes clear  
678 that the decrease in density is probably attributed, at least partially, to erosion of the  
679 upper layers. However, it is also likely that snowfall at low wind speeds contributed to  
680 a reduction in density, as well, which occurred between 29 and 30 Jan (Fig. 12g). In con-  
681 trast to 30 Jan, the mean density of the entire profile increased between 16 Jan and 6  
682 Feb. At the same time, the mean height has decreased, but only by 4.3 cm on average.  
683 This corresponds to an increase of 3 cm compared to 30 Jan.

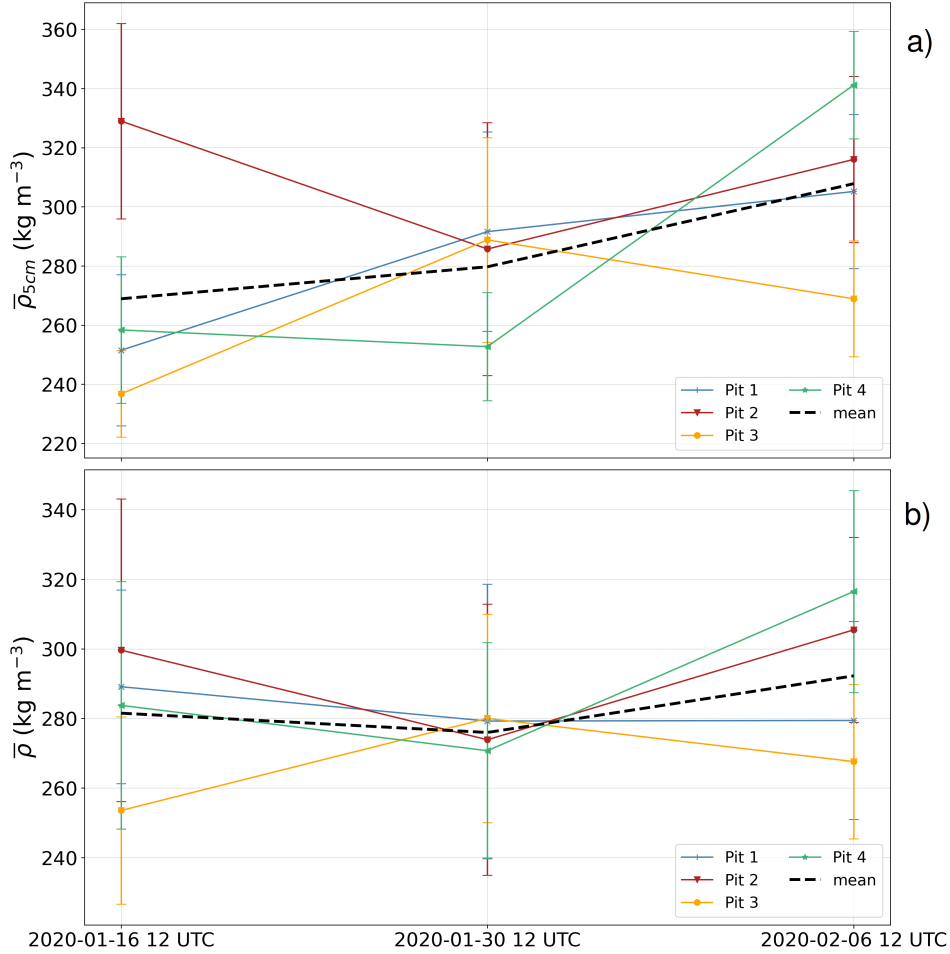


**Figure 14.** a) Averaged snow surface densities (upper 5 cm) for snow pits 1–4. The black dashed line notes the total average over time. Error bars show the corresponding upper and lower limit for the standard deviation at each pit location at each time. b) same as in a) but averaged for the whole vertical profile.

### 3.3.2 Modeled snow density

We now analyse if the model is able to reproduce the  $\bar{\rho}_{5cm}$  increase with time found in the manual snow pits. Spatially modeled snow density fields for the top 5 cm of the snowpack,  $\bar{\rho}_{5cm}$ , for R and C simulations, respectively, are shown in Fig.10c and Fig.10d. Spatial differences of the density between R and C are visible. For the C scenario, the density is higher on average, and the surface appears smoother, while for the R scenario, the spatial variation appears larger with lower maximum densities.

As discussed in the previous section, the smaller fluid threshold in scenario R increases snow transport and consequently increases the spatial snow distribution. There is also a significant increase in  $\bar{\rho}_{5cm}$  with time (Fig. 12e, Tab. 1). SMP-based horizontally averaged  $\bar{\rho}_{5cm}$  and their respective standard deviations are shown for 16 Jan, 30 Jan and 6 Feb in the same figure. Most of the time, in the C scenario, the surface density is slightly higher. While during the first event the densities increase to approximately the same value of slightly over 280 kg m<sup>-3</sup>. Subsequently, the R scenario density drops to lower values. At a later time, during the snowfall event, the densities are almost equal again, and this behaviour continues. At the beginning of the simulation period, the den-

700 city is about the same as the measurements on 16 Jan ( $269 \text{ kg m}^{-3}$ ). The reason for this  
 701 is that the 1-D SNOWPACK model was initiated with the density measurements on 16  
 702 Jan, and during the spin-up period of 10 days until 26 Jan (Fig. 4). Accordingly, the sur-  
 703 face density remained about the same between 16 Jan and 26 Jan (which also justifies  
 704 a comparison of the measurements from 16 Jan with the model on 26 Jan, also regard-  
 705 ing snow depth and SWE). On 30 Jan, the measured average is  $280 \text{ kg m}^{-3}$ , which is well  
 706 captured by the R scenario, where the C scenario models slightly too high values. By  
 707 the end of the simulation, neither simulation correctly reproduces the averaged measured  
 708 density ( $308 \text{ kg m}^{-3}$ ); however, both models are within the lower standard deviation of  
 709 the measurement. The R scenario generally shows a stronger variability of the density  
 710 with time, in particular it shows stronger decreases in the intermediate time. Here, we  
 711 note that the modeled average surface density may decrease significantly with time due  
 712 to 3 reasons:

- 713 1. Due to snowfall during low wind speeds, which produces low density layers on top.
- 714 2. When at certain locations in the domain the wind speed is sufficient to generate  
 715 snow transport, i.e. when the threshold friction velocity  $u_{*th}$  is exceeded, while at  
 716 the same time, the deposited snow density function (Equation 1) computes rel-  
 717 atively low densities for the re-deposition of the snow that has been eroded from  
 718 high-density surfaces. This might lead to a decrease, on average.
- 719 3. When erosion may expose lighter layers lower down in the snow cover.

720 The difference between the R and C simulations is attributed to point 2, as the snow-  
 721 fall rate and wind speed are identical for both scenarios. An increased  $u_{*th}$  leads to less  
 722 re-distribution and hence less fluctuation in the density. However, the significant drop  
 723 of  $\bar{\rho}_{5cm}$  for both scenarios - R and C - is attributed to snowfall (explained under point  
 724 1 above), as snowfall occurred before the wind started on 1 Feb. Interestingly,  $\bar{\rho}_{5cm}$  of  
 725 the R and C scenario converge during the subsequent event with the highest measured  
 726 wind speed on 1 Feb, which occurred under significant snowfall conditions.

### 727 *3.3.3 Comparison with 1-D SNOWPACK simulations*

728 To evaluate whether a time- and computationally intensive calculation with ALPINE3D  
 729 gives an advantage in terms of averaged properties over very short time and low com-  
 730 putationally intensive 1-dimensional simulations, we compared two SNOWPACK sim-  
 731 ulations, R\_SP and C\_SP with ALPINE3D R and C. The  $\bar{\rho}_{5cm}$  time series shown in Fig. 12e),  
 732 reveal that neither of the two SNOWPACK setups is able to simulate the  $\bar{\rho}_{5cm}$  increase  
 733 on 30 Jan 1200 UTC. For the measurement at this time, the density is underestimated  
 734 for SP\_R by  $8 \text{ kg m}^{-3}$  and for SP\_C by  $13 \text{ kg m}^{-3}$ . In contrast to that, the R and C sce-  
 735 narios of ALPINE3D show an excellent agreement for  $\bar{\rho}_{5cm}$  with the measurements at  
 736 this time. However, by the end of the simulation period neither one of the A3D simu-  
 737 lations nor one of the SNOWPACK simulations captures the average measured density  
 738 accurately. However, SP\_R is closest to the measured  $\bar{\rho}_{5cm}$ , while SP\_C is similar to C.  
 739 This is somewhat surprising, as intuitively, we would have expected that a decreased fluid  
 740 threshold would lead to more erosion, and consequently a decreased  $\bar{\rho}_{5cm}$ .

741 Unlike the A3D setups, neither of the SNOWPACK simulations shows lots of vari-  
 742 ability with time. All of the modeled densities lay within the lower standard deviation  
 743 of the measured density. While the differences in results between SP\_R and SP\_C are  
 744 quite high at the end of the simulation time, they are smaller for the same change in the  
 745  $\alpha$  parameter. Based on these findings, one could perhaps argue that using ALPINE3D  
 746 with the snowdrift module reduces the probability of being way off in the results. The  
 747 temporal fluctuation of  $\bar{\rho}_{5cm}$  in the ALPINE3D setups may not seem realistic, but it is  
 748 at least as questionable how likely it is that - as simulated by SNOWPACK - there is  
 749 almost no fluctuation except for very punctual events.

750

### 3.4 Cross sections

751

752

753

754

755

756

757

758

In a final step, we evaluate the model in terms of snow deposition in detailed cross sections. Cross sections in typical wind-erosion/deposition areas allow for a detailed investigation, for instance in terms of snow height, grain ratios, snow age, density or thermal conductivity. This is particularly interesting when considering that the model in its current state does not form dunes on level areas. In addition, considering that ridges are main accumulation zones, the cross sections might show a potential to investigate thermodynamic ice growth in these areas in future work. The located cross sections are shown in Fig. 11 as sections 1–3 (S1–S3)

759

#### *S1*

760

761

762

763

764

765

766

S1 is the cross section where the model reproduced erosion and deposition in best agreement with TLS measurements (Fig. 15a). It is noteworthy that this section is characterized first and foremost by the fact that it is aligned approximately  $90^\circ$  to a distinct pressure ridge of about 1 m height. The model reproduces here the snow depth difference very well, and the most pronounced difference is that it computes a sharp accumulation peak on top of the ridge that is not seen in the measurements (Fig. 15a). On the other hand, the model also reproduces the depth decrease at approximately 10 m distance.

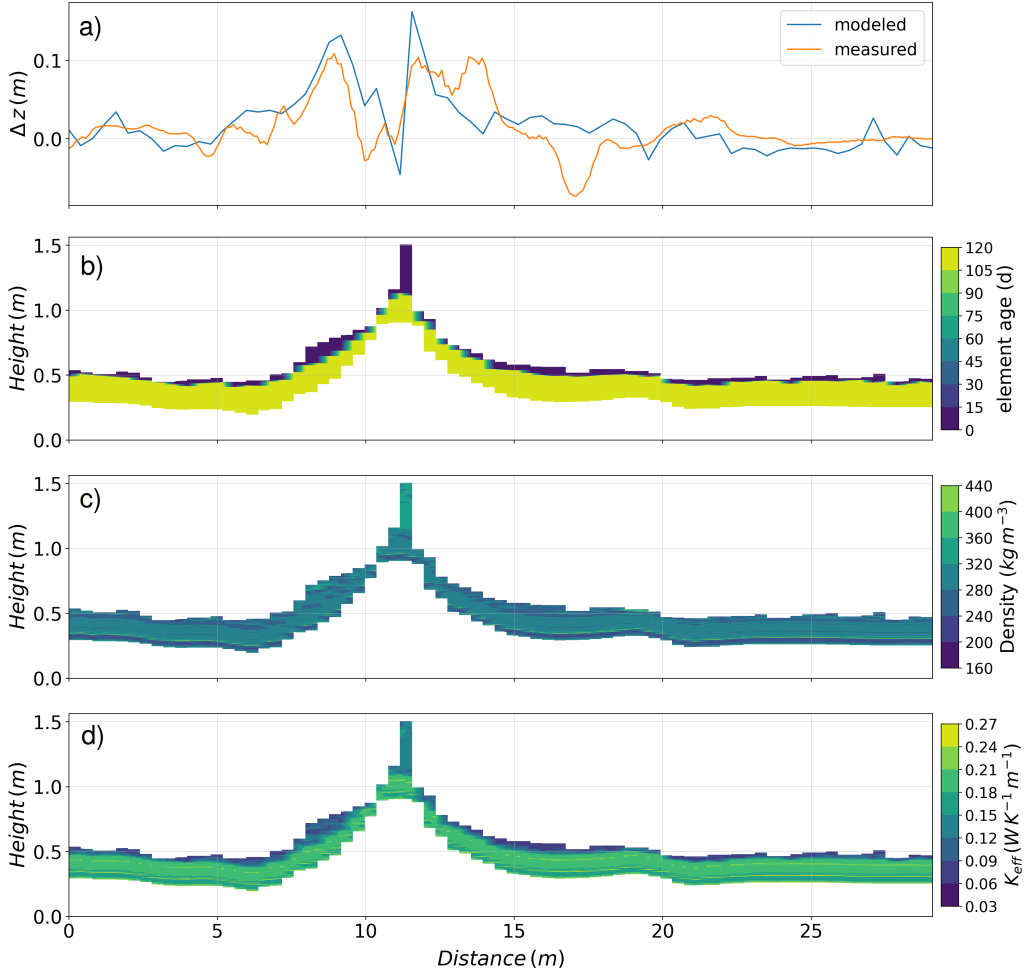


**Figure 15.** Cross section plots related to cross section 1 (S1) of the reference simulation (R), as shown in Fig. 11, of a) snow depth difference (4 Feb – 25 Jan) of the model output and TLS, b) snow age, c) snow density and d) thermal conductivity of snow.

767 Fig. 15d shows that most of the snow has been accumulated in approximately the  
 768 last three days in the model run, which corresponds to the time period 1 – 4 Feb. For  
 769 the same period, the highest densities of deposited snow are computed (Fig. 15c).

770 Detailed computed thermal conductivities (Fig. 15d) show the potential of the model.  
 771 The modeled values of the deposited snow on top are probably too low here, as Macfarlane  
 772 et al. (2023) found an time-and spatial average  $K_{\text{eff}}$  of  $0.25 \pm 0.05 \text{ W K}^{-1} \text{ m}^{-1}$  for MO-  
 773 SAiC. Reasons for the low modeled  $K_{\text{eff}}$  are not known at this time, and need to be re-  
 774 searched further. Macfarlane et al. (2023) also state that the thermal conductivity of snow  
 775 around ridges does not significantly differ from snow on level areas, however, they found  
 776 that the thermal resistance instead was about 3 times higher on ridges areas and they  
 777 conclude that therefore ridges should be separately considered for modeling. This find-  
 778 ing and the ability of our model to represent the thermal properties of snow in spatial  
 779 detail reinforces our approach.

780

**S2**

781

782

783

The detailed cross section 2 is shown in Fig. 16. While on the ridged area right to the highest point of the ridge at approximately 18 cm distance, the model accumulates too much snow, the snow height is accurately modeled left of the ridge peak (Fig. 16a).

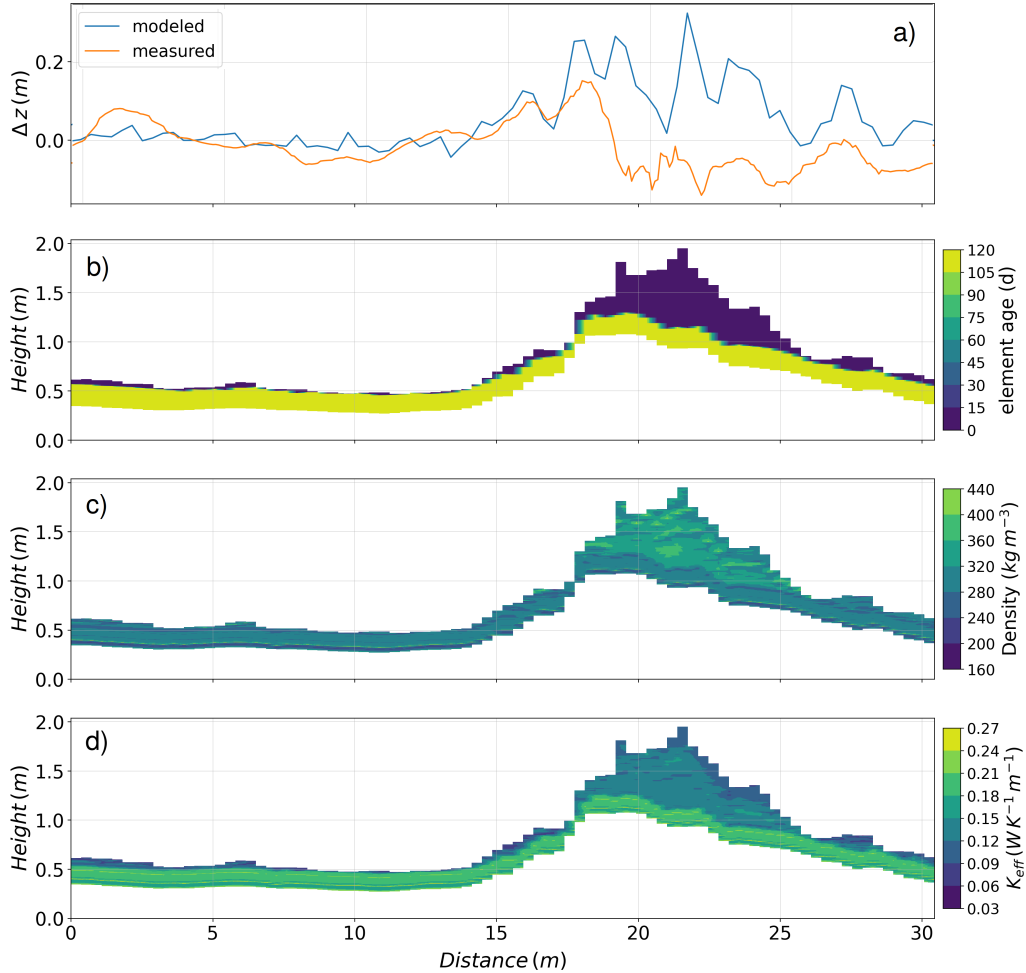


**Figure 16.** As in Fig. 15, but for cross section S2 as shown in Fig. 11.

784

785

786

787

788

789

The colours in the snow age (Fig. 16a) indicate, that most of the deposition occurred during one event. In the large accumulation between around 17 and 20 m distance, a strong spatial variability in density is observed (Fig. 16c), clearly showing the increased density of the freshly deposited snow.  $K_{eff}$  (Fig. 16d) again shows quite low values which need to be investigated. The large snow accumulation highlights why the thermal resistance can be large around ridges (Macfarlane et al., 2023).

790

**S3**

791

792

793

794

In cross section 3, we wanted to investigate the highly variable accumulation in form of waves that was observed (Fig. 11b,d). The spatial variability of the measurement is seen in Fig. 17a. The model does not model these highly accurately, however, it appears like there is a correlation, and that mainly the phase is shifted, especially for the first

795 10 m. Generally, the model reproduces here the differences well. Fig. 17b reveals that  
 796 the snow accumulation occurred much more homogeneously compared to cross section  
 797 1 and 2. This shows that a flat surface tends to lead to more homogeneous accumula-  
 798 tion, contrary to ridged areas.

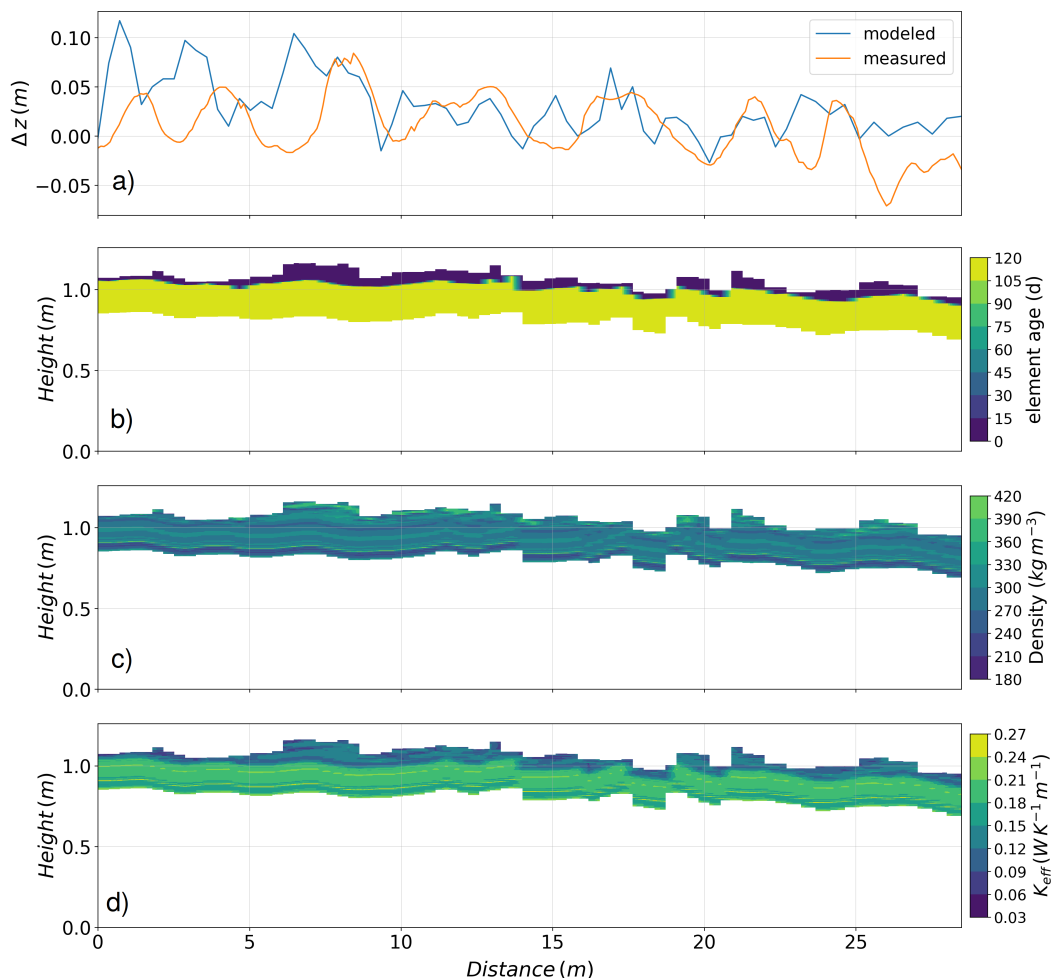


**Figure 17.** As in Fig. 15, but for cross section S3 as shown in Fig. 11.

799 The density (Fig. 17c) and thermal conductivity (Fig. 17d) reveal not many large  
 800 conspicuities compared to cross section 1 and cross section 2.

#### 801 4 Conclusions and Outlook

802 We applied the 3D-snow cover-atmosphere model ALPINE3D with the drifting snow  
 803 module to Arctic sea ice for the first time, for an area of 100 x 100 m. The fitted model  
 804 simulated a 10-day simulation period in which the model would be fed by measurement  
 805 data collected during the winter of the Multidisciplinary drifting Observatory for the Study  
 806 of Arctic Climate expedition (MOSAIC). A digital elevation model (DEM) was used as  
 807 the underlying topography, based on terrestrial laser scans (TLS) conducted during the  
 808 expedition. As wind field input, we used RANS steady state wind fields computed with  
 809 OpenFOAM based on in-situ measurements of wind speed and direction, collected on  
 810 a meteorological tower. Other measurement data from and around the tower used to drive

811 the model were air temperature, relative humidity and incoming longwave radiation. Snow  
 812 depth and detailed snow density measurements were used to initialise and evaluate the  
 813 model. For comparison of the modeled mass fluxes, horizontal mass fluxes derived from  
 814 a Snow Particle Counter (SPC) measurement at the meteorological tower were used. Af-  
 815 ter calibration, we conducted a sensitivity study, with respect to an increased fluid thresh-  
 816 old. In addition, we made comparisons with 1-D SNOWPACK simulations. A detailed  
 817 study of spatio-temporal snow-redistribution and surface snow densification has been con-  
 818 ducted. Finally, detailed snow profiles along three selected cross sections in the domain  
 819 were investigated.

820 The model shows a very good timing for snow transport compared to measurements  
 821 and estimates relative mass fluxes well with high correlation of  $r = 0.92$ . The histograms  
 822 of the snow depth differences do not deviate largely from the measurements, but when  
 823 using an increased fluid threshold, the compression of the distribution gets significantly  
 824 decreased - which is due to a reduced wind-induced transport of snow. When looking  
 825 at the spatial correlation in the form of a semi-variogram, it is noticeable that generally  
 826 the modeled semi-variance is significantly higher than the measured - however, the range  
 827 of 6 m is about the same for both the model and the measurements. Interestingly, Liston  
 828 et al. (2018) also found a range of 6 m (for measurements of absolute height), and Sturm  
 829 et al. (2002) found values at least close to 6 m. The initially strongly increasing semi-  
 830 variance in the model in the lower range is probably due to the missing generation of dunes,  
 831 which can be clearly seen in the measurements. Using time series of statistical snow dis-  
 832 tribution, we were able to visualize the wind-induced redistribution of snow. These show  
 833 that significantly less snow redistribution occurs when the fluid threshold is increased.  
 834 While in the reference simulation redistribution occurs almost continuously, in the com-  
 835 parison scenario redistribution can essentially be reduced to the four events that stand  
 836 out clearly from the measurements. The qualitative comparisons between model and mea-  
 837 surements show that dunes are hardly formed in the model, which is probably due to a  
 838 missing dynamic mesh in the model, as the near-surface wind field does not adapt to the  
 839 freshly deposited snow from the previous period. However, there are some areas where  
 840 the model reproduces the accumulation excellently, and even if on a very small scale matches  
 841 do not necessarily prevail, the model calculates large amounts of snow - as in the mea-  
 842 surements - in the ridged areas. Erosion occurs in the model, but is generally underes-  
 843 timated compared to the measurements.

844 The time course of the spatially averaged surface density of the upper 5 cm shows  
 845 that wind slab formed, with a value of  $269 \text{ kg m}^{-3}$  on 16 Jan,  $280 \text{ kg m}^{-3}$  on 30 Jan, and  
 846  $308 \text{ kg m}^{-3}$  on 6 Feb, becoming increasingly stronger. The averaged density over the en-  
 847 tire profile, unlike the surface density, shows a decrease at 30 Jan, while it increases again  
 848 at 6 Feb. The reason is probably that as erosion increased, the density fraction of lay-  
 849 ers below, consisting mostly of depth hoar or faceted grains, increased relatively within  
 850 the mean. The averaged surface density in the model is excellently reproduced at 30 Jan,  
 851 but at 6 Feb it is underestimated by  $26 \text{ kg m}^{-3}$  in R and by  $22 \text{ kg m}^{-3}$  in C, although  
 852 both modeled means are still within the standard deviation of the measurements. SNOW-  
 853 PACK, on the other hand, models a too low density at 30 Jan (R underestimated by  $15 \text{ kg m}^{-3}$ ;  
 854 C underestimated by  $13 \text{ kg m}^{-3}$ ), while it is closer to the measurements, at least with  
 855  $\alpha$  of 3.0 at 6 Feb (reference underestimated by  $8 \text{ kg m}^{-3}$ ; comparison underestimated by  
 856  $28 \text{ kg m}^{-3}$ ). The temporal variation of the density is significantly higher for ALPINE3D  
 857 than for SNOWPACK, which is especially the case for the reference. The strong decreases  
 858 in densities at times are rather unrealistic and due to the fact that in the current set-  
 859 tings the model erodes too easily at low fluid threshold, and then calculates too low den-  
 860 sities with the given density parameterization for just deposited snow, which corresponds  
 861 to a decrease in density on average. Overall, the differences between the two ALPINE3D  
 862 setups are smaller than between the two SNOWPACK setups, leading us to conclude that  
 863 using an ALPINE3D drifting snow setup reduces the likelihood of being wrong with an  
 864 adjusted fluid threshold.

865 The cross sections reveal details of deposition and erosion, both in terms of height  
 866 differences between model and simulation, as well as spatially high-resolution param-  
 867 eters, such as age of the deposited snow, density, or thermal conductivity. For the selected  
 868 cross sections 1-3, the model simulates the snow depth differences extremely well for the  
 869 most part, especially for cross section 1. However, the visible correlations in cross sec-  
 870 tions 2 and 3, as well as the accurately calculated snow depth difference left of the ridge  
 871 cross section 2 are also remarkable. The observed waves in cross section 3 are not clearly  
 872 reproduced, but it is apparently phase-shifted at a similar wave-length. The snow age  
 873 in the cross sections allows to investigate when the snow has settled. The density in the  
 874 cross sections reveal stronger spatial variations for the snow that has accumulated over  
 875 time. The plots of the effective thermal conductivity show - even if the conductivity of  
 876 the freshly deposited snow appears too high (under the assumption of drifting snow)  
 877 - how the effects of the snow cover on sea ice growth in ridged areas could be investigated.

878 Our adjusted ALPINE3D setup using the snowdrift routine with RANS wind fields  
 879 and a high resolution sea ice topography, allows for detailed investigation of the Arctic  
 880 snow cover. For the first time, snow redistribution on sea ice is modeled in dependence  
 881 of temporally varying detailed snow properties. This approach could be particularly rel-  
 882 evant for modeling during highly variable weather, e.g., storms or warm air intrusions  
 883 (Liston et al., 2007), because it then causes the microstructure of the snow surface to  
 884 change significantly with time due to sintering. An Arctic undergoing major climatic changes  
 885 with increasing temperatures increases this demand. We see several applications as well  
 886 as further developments in the future. A combination of our setup with the sea ice vari-  
 887 ant of ALPINE3D (Wever et al., 2020, 2021) could allow a detailed study of the spatial  
 888 variability of the thermodynamically driven growth and melt of sea ice. By studying our  
 889 cross sections, we have already shown an approach to conduct this, e.g., it would be pos-  
 890 sible to study the effect of the effective thermal conductivity of snow on the ice growth  
 891 on and around pressure ridges. Furthermore, we believe that a dynamic mesh would again  
 892 greatly improve the model, allowing for dune formation. In combination with the gen-  
 893 eral approach to study sea ice mass balances, this would be of great relevance e.g. for  
 894 the formation of melt ponds (Petrich et al., 2012; Lecomte et al., 2015). However, dunes  
 895 could also be generated, for example, within a sub-model using a cellular automaton (Sharma  
 896 et al., 2019). For a better evaluation of the model, we recommend higher temporal res-  
 897 olution TLS, as well as higher spatial and temporal resolution measurements of snow prop-  
 898 erties in future measurement campaigns.

## 899 5 Open Research

900 A3D and SNOWPACK Setup data (include OpenFOAM generated wind fields) are  
 901 available at <https://doi.org/10.5281/zenodo.7723224> (Wagner & Lehning, 2023).  
 902 TLS point clouds can be obtained from <https://arcticdata.io/data/10.18739/A26688K9D/>  
 903 (Clemens-Sewall et al., 2023). The flux tower wind measurements can be downloaded  
 904 from [ftp://ftp2.psl.noaa.gov/Projects/MOSAIC/tower/3\\_level\\_archive/level3](ftp://ftp2.psl.noaa.gov/Projects/MOSAIC/tower/3_level_archive/level3)  
 905 [.4/](https://doi.org/10.5439/1498936), (Cox et al., 2023). KAZR data can be obtained from the ARM data center: [https://](https://doi.org/10.5439/1498936)  
 906 [doi.org/10.5439/1498936](https://doi.org/10.5439/1498936) (Lindenmaier et al., 2020). All SMP profiles are available  
 907 on <https://doi.org/10.1594/PANGAEA.935554> (Macfarlane et al., 2021). Transect Mag-  
 908 naprobe snow depths can be downloaded from <https://doi.org/10.1594/PANGAEA.937781>  
 909 (Itkin et al., 2021). SWE derived from Transect and SMP can be downloaded under [https://](https://doi.pangaea.de/10.1594/PANGAEA.927460)  
 910 [doi.pangaea.de/10.1594/PANGAEA.927460](https://doi.pangaea.de/10.1594/PANGAEA.927460) (Wagner et al., 2021). Preliminary SPC data  
 911 can be obtained from <https://doi.org/10.5281/zenodo.7715728> (Wagner & Frey, 2023).  
 912 Source code for the adjusted ALPINE3D model can be obtained from [https://gitlabext](https://gitlabext.wsl.ch/snow-models/alpine3d.git)  
 913 [.wsl.ch/snow-models/alpine3d.git](https://gitlabext.wsl.ch/snow-models/alpine3d.git) under the "alpine3d\_mosaic" branch. Source code  
 914 for the adjusted SNOWPACK model can be obtained from [https://gitlabext.wsl.ch/](https://gitlabext.wsl.ch/snow-models/snowpack.git)  
 915 [snow-models/snowpack.git](https://gitlabext.wsl.ch/snow-models/snowpack.git) under the "snowpack\_mosaic" branch. The source code for

916 OpenFOAM® v2106 can be downloaded from [https://develop.openfoam.com/Development/](https://develop.openfoam.com/Development/openfoam.git)  
 917 [openfoam.git](https://develop.openfoam.com/Development/openfoam.git).

## 918 Acknowledgments

919 David N. Wagner and Michael Lehning were supported by the Swiss National Science  
 920 Foundation (grant no. SNSF-200020\_179130). Martin Schneebeli, Amy R. Macfarlane  
 921 and David N. Wagner were supported by the Swiss Polar Institute (grant no. DIRCR-  
 922 2018-003). Martin Schneebeli and Amy R. Macfarlane were supported by the European  
 923 Union’s Horizon 2020 research and innovation program projects ARICE (grant no. 730965)  
 924 for berth fees associated with the participation of the DEARice project and the WSL  
 925 Institute for Snow and Avalanche Research SLF (grant no. WSL\_201812N1678). David  
 926 Clemens-Sewall was supported by NSF OPP-1724540. Matthew D. Shupe was supported  
 927 by the DOE Atmospheric System Research Program (grant nos. DE-SC0019251 and DE-  
 928 SC0021341). Data used in this paper were produced as part of the international Mul-  
 929 tidisciplinary drifting Observatory for the Study of the Arctic Climate (MOSAiC) with  
 930 the tag MOSAIC20192020 and the project ID: AWI\_PS122\_00. Met tower data were sup-  
 931 ported by the National Science Foundation (grant no. OPP-1724551) and by NOAA’s  
 932 Physical Sciences Laboratory (PSL) and Global Ocean Monitoring and Observing Pro-  
 933 gram (GOMO). KAZR reflectivities for precipitation retrieval were obtained from the  
 934 Atmospheric Radiation Measurement (ARM) user facility, a U.S. Department of Energy  
 935 (DOE) Office of Science user facility managed by the Biological and Environmental Re-  
 936 search Program. The authors thank all MOSAiC participants for contributing to the pa-  
 937 per in one way or another: the MOSAiC logistics team, the ship’s personnel, all the dif-  
 938 ferent team members (ICE, ATMOS, BGC, ECO, OCEAN), the ARM crew, the project  
 939 coordination and the MOSAiC project board. We also refer to the extended acknowl-  
 940 edgement for MOSAiC (Nixdorf et al., 2021). We thank Daniel Kükenbrink for the help-  
 941 ful information on proper point cloud processing with open source software.

## 942 References

- 943 Bagnold, R. A. (1941). *The physics of blown sand and desert dunes / by r.a. bagnold*  
 944 [Book]. William Morrow New York.
- 945 Bartelt, P., & Lehning, M. (2002). A physical SNOWPACK model for the Swiss  
 946 avalanche warning Part I: numerical model. *Cold Regions Science and Technol-*  
 947 *ogy*, 35(3), 123–145. doi: 10.1016/s0165-232x(02)00074-5
- 948 Blackford, J. R. (2007, oct). Sintering and microstructure of ice: a review. *Journal*  
 949 *of Physics D: Applied Physics*, 40(21), R355–R385. Retrieved from [https://](https://doi.org/10.1088%2F0022-3727%2F40%2F21%2Fr02)  
 950 [doi.org/10.1088%2F0022-3727%2F40%2F21%2Fr02](https://doi.org/10.1088%2F0022-3727%2F40%2F21%2Fr02) doi: 10.1088/0022-3727/  
 951 40/21/r02
- 952 Clemens-Sewall, D., Polashenski, C., Raphael, I., Perovich, D., Fons, S., Itkin, P., ...  
 953 Svavarsdottir, S. (2023). *High-resolution repeat topography of drifting ice floes*  
 954 *in the arctic ocean from terrestrial laser scanning collected on the multidisci-*  
 955 *plinary drifting observatory for the study of arctic climate expedition*. [Data  
 956 set]. (Arctic Data Center.) doi: 10.18739/A26688K9D
- 957 Clifton, A., Rüedi, J.-D., & Lehning, M. (2006). Snow saltation threshold measure-  
 958 ments in a drifting-snow wind tunnel. *Journal of Glaciology*, 52(179), 585–596.  
 959 doi: 10.3189/172756506781828430
- 960 CloudCompare. (2023). *Cloudcompare source code*. Retrieved from [https://github](https://github.com/CloudCompare/CloudCompare)  
 961 [.com/CloudCompare/CloudCompare](https://github.com/CloudCompare/CloudCompare)
- 962 Colbeck, S. (1998). Sintering in a dry snow cover. *Journal of Applied Physics*,  
 963 84(8), 4585-4589. Retrieved from <https://doi.org/10.1063/1.368684> doi:  
 964 10.1063/1.368684
- 965 Colbeck, S., of Engineers, U. S. A. C., Research, C. R., & (U.S.), E. L. (1997). *A re-*  
 966 *view of sintering in seasonal snow*. U.S. Army Cold Regions Research and En-

- 967           gineering Laboratory. Retrieved from [https://books.google.ch/books?id=D\\\_CHKAAACAAJ](https://books.google.ch/books?id=D\_CHKAAACAAJ)
- 968
- 969 Conrad, O., Bechtel, B., Bock, M., Dietrich, H., Fischer, E., Gerlitz, L., ...
- 970 Böhner, J. (2015). System for automated geoscientific analyses (saga)
- 971 v. 2.1.4. *Geoscientific Model Development*, 8(7), 1991–2007. Retrieved
- 972 from <https://gmd.copernicus.org/articles/8/1991/2015/> doi:
- 973 10.5194/gmd-8-1991-2015
- 974 Cox, C., Gallagher, M., Shupe, M., Persson, O., Solomon, A., Fairall, C., ... Uttal,
- 975 T. (2023). *Continuous observations of the surface energy budget and meteorol-*
- 976 *ogy over the arctic sea ice during mosaic.* (Multidisciplinary Drifting Observa-
- 977 *tory for the Study of Arctic Climate (MOSAIC), central Arctic, October 2019 -*
- 978 *September 2020. Scientific Data. Submitted.)* doi: 10.18739/A2PV6B83F
- 979 Déry, S. J., & Tremblay, L.-B. (2004). Modeling the effects of wind redis-
- 980 *tribution on the snow mass budget of polar sea ice.* *Journal of Physi-*
- 981 *cal Oceanography*, 34(1), 258–271. Retrieved from [https://doi.org/](https://doi.org/10.1175/1520-0485(2004)034<0258:MTEOWR>2.0.CO;2)
- 982 [10.1175/1520-0485\(2004\)034<0258:MTEOWR>2.0.CO;2](https://doi.org/10.1175/1520-0485(2004)034<0258:MTEOWR>2.0.CO;2) doi: 10.1175/
- 983 1520-0485(2004)034(0258:MTEOWR)2.0.CO;2
- 984 Doorschot, J. J. J., & Lehning, M. (2002). Equilibrium saltation: Mass fluxes, aero-
- 985 *dynamic entrainment, and dependence on grain properties.* *Boundary-Layer*
- 986 *Meteorology*, 104(1), 111–130. doi: 10.1023/a:1015516420286
- 987 Doorschot, J. J. J., Lehning, M., & Vrouwe, A. (2004, Dec 01). Field measure-
- 988 *ments of snow-drift threshold and mass fluxes, and related model simulations.*
- 989 *Boundary-Layer Meteorology*, 113(3), 347–368. Retrieved from [https://](https://doi.org/10.1007/s10546-004-8659-z)
- 990 [doi.org/10.1007/s10546-004-8659-z](https://doi.org/10.1007/s10546-004-8659-z) doi: 10.1007/s10546-004-8659-z
- 991 Fierz, C., Armstrong, R., Durand, Y., Etchevers, P., Greene, E., Mcclung, D., ...
- 992 Sokratov, S. (2008, 09). The 2008 international classification of seasonal snow
- 993 *on the ground.* In (p. 579–580).
- 994 Filhol, S., & Sturm, M. (2015). Snow bedforms: A review, new data, and a for-
- 995 *mation model.* *Journal of Geophysical Research: Earth Surface*, 120(9), 1645-
- 996 1669. Retrieved from [https://agupubs.onlinelibrary.wiley.com/doi/abs/](https://agupubs.onlinelibrary.wiley.com/doi/abs/10.1002/2015JF003529)
- 997 [10.1002/2015JF003529](https://doi.org/10.1002/2015JF003529) doi: <https://doi.org/10.1002/2015JF003529>
- 998 Gerber, F., Lehning, M., Hoch, S. W., & Mott, R. (2017). A close-ridge small-scale
- 999 *atmospheric flow field and its influence on snow accumulation.* *Journal of Geo-*
- 1000 *physical Research: Atmospheres*, 122(15), 7737–7754. Retrieved from [https://](https://agupubs.onlinelibrary.wiley.com/doi/abs/10.1002/2016JD026258)
- 1001 [agupubs.onlinelibrary.wiley.com/doi/abs/10.1002/2016JD026258](https://agupubs.onlinelibrary.wiley.com/doi/abs/10.1002/2016JD026258) doi:
- 1002 <https://doi.org/10.1002/2016JD026258>
- 1003 Groot Zwaaftink, C. D., Cagnati, A., Crepaz, A., Fierz, C., Macelloni, G., Valt, M.,
- 1004 & Lehning, M. (2013, 02). Event-driven deposition of snow on the antarctic
- 1005 *plateau: Analyzing field measurements with snowpack.* *The Cryosphere,*
- 1006 *Volume 7, Issue 1, 2013, pp.333-347*, 7, 333–347. doi: 10.5194/tc-7-333-2013
- 1007 Groot Zwaaftink, C. D., Diebold, M., Horender, S., Overney, J., Lieberherr, G.,
- 1008 Parlange, M. B., & Lehning, M. (2014, Oct 01). Modelling small-scale drift-
- 1009 *ing snow with a lagrangian stochastic model based on large-eddy simulations.*
- 1010 *Boundary-Layer Meteorology*, 153(1), 117–139. Retrieved from [https://](https://doi.org/10.1007/s10546-014-9934-2)
- 1011 [doi.org/10.1007/s10546-014-9934-2](https://doi.org/10.1007/s10546-014-9934-2) doi: 10.1007/s10546-014-9934-2
- 1012 Hames, O., Jafari, M., Wagner, D. N., Raphael, I., Clemens-Sewall, D., Polashen-
- 1013 *ski, C., ... Lehning, M. (2022). Modeling the small-scale deposition of*
- 1014 *snow onto structured arctic sea ice during a mosaic storm using snowbed-*
- 1015 *foam 1.0.* *Geoscientific Model Development*, 15(16), 6429–6449. Retrieved
- 1016 from <https://gmd.copernicus.org/articles/15/6429/2022/> doi:
- 1017 10.5194/gmd-15-6429-2022
- 1018 Itkin, P., Webster, M., Hendricks, S., Oggier, M., Jaggi, M., Ricker, R., ... Liston,
- 1019 G. E. (2021). *Magnaprobe snow and melt pond depth measurements from the*
- 1020 *2019-2020 mosaic expedition.* (PANGAEA) doi: 10.1594/PANGAEA.937781
- 1021 Juretic, F., Philippose, R., & Clifford, I. (2021). *cfmesh source code.* Retrieved from

- 1022 <https://sourceforge.net/p/cfmesh/code/ci/development/tree/>
- 1023 Keenan, E., Wever, N., Dattler, M., Lenaerts, J. T. M., Medley, B.,  
1024 Kuipers Munneke, P., & Reijmer, C. (2021). Physics-based snowpack model  
1025 improves representation of near-surface antarctic snow and firn density. *The*  
1026 *Cryosphere*, *15*(2), 1065–1085. Retrieved from [https://tc.copernicus.org/](https://tc.copernicus.org/articles/15/1065/2021/)  
1027 [articles/15/1065/2021/](https://tc.copernicus.org/articles/15/1065/2021/) doi: 10.5194/tc-15-1065-2021
- 1028 King, J., Howell, S., Brady, M., Toose, P., Derksen, C., Haas, C., & Beckers,  
1029 J. (2020). Local-scale variability of snow density on Arctic sea ice. *The*  
1030 *Cryosphere*, *14*(12), 4323–4339. doi: 10.5194/tc-14-4323-2020
- 1031 Lecomte, O., Fichfet, T., Flocco, D., Schroeder, D., & Vancoppenolle, M.  
1032 (2015). Interactions between wind-blown snow redistribution and melt  
1033 ponds in a coupled ocean–sea ice model. *Ocean Modelling*, *87*, 67–80. Re-  
1034 trieved from [https://www.sciencedirect.com/science/article/pii/](https://www.sciencedirect.com/science/article/pii/S1463500314001784)  
1035 [S1463500314001784](https://www.sciencedirect.com/science/article/pii/S1463500314001784) doi: <https://doi.org/10.1016/j.ocemod.2014.12.003>
- 1036 Lee, S., Wolberg, G., & Shin, S. (1997). Scattered data interpolation with multilevel  
1037 b-splines. *IEEE Transactions on Visualization and Computer Graphics*, *3*(3),  
1038 228–244. doi: 10.1109/2945.620490
- 1039 Lehning, M., Bartelt, P., Brown, B., Fierz, C., & Satyawali, P. (2002). A physical  
1040 snowpack model for the swiss avalanche warning: Part ii. snow microstruc-  
1041 ture. *Cold Regions Science and Technology*, *35*(3), 147 - 167. Retrieved from  
1042 <http://www.sciencedirect.com/science/article/pii/S0165232X02000733>  
1043 doi: [https://doi.org/10.1016/S0165-232X\(02\)00073-3](https://doi.org/10.1016/S0165-232X(02)00073-3)
- 1044 Lehning, M., Bartelt, P., Brown, B., Russi, T., Stöckli, U., & Zimmerli, M. (1999).  
1045 snowpack model calculations for avalanche warning based upon a new net-  
1046 work of weather and snow stations. *Cold Regions Science and Technol-*  
1047 *ogy*, *30*(1), 145 - 157. Retrieved from [http://www.sciencedirect.com/](http://www.sciencedirect.com/science/article/pii/S0165232X99000221)  
1048 [science/article/pii/S0165232X99000221](http://www.sciencedirect.com/science/article/pii/S0165232X99000221) doi: [https://doi.org/10.1016/](https://doi.org/10.1016/S0165-232X(99)00022-1)  
1049 [S0165-232X\(99\)00022-1](https://doi.org/10.1016/S0165-232X(99)00022-1)
- 1050 Lehning, M., Löwe, H., Ryser, M., & Raderschall, N. (2008). Inhomogeneous precip-  
1051 itation distribution and snow transport in steep terrain. *Water Resources Re-*  
1052 *search*, *44*(7). Retrieved from [https://agupubs.onlinelibrary.wiley.com/](https://agupubs.onlinelibrary.wiley.com/doi/abs/10.1029/2007WR006545)  
1053 [doi/abs/10.1029/2007WR006545](https://agupubs.onlinelibrary.wiley.com/doi/abs/10.1029/2007WR006545) doi: 10.1029/2007WR006545
- 1054 Lehning, M., Völksch, I., Gustafsson, D., Nguyen, T. A., Stähli, M., & Zappa, M.  
1055 (2006). Alpine3d: a detailed model of mountain surface processes and its appli-  
1056 cation to snow hydrology. *Hydrological Processes*, *20*(10), 2111–2128. Retrieved  
1057 from <https://onlinelibrary.wiley.com/doi/abs/10.1002/hyp.6204> doi:  
1058 [10.1002/hyp.6204](https://onlinelibrary.wiley.com/doi/abs/10.1002/hyp.6204)
- 1059 Leonard, K. C., & Maksym, T. (2011). The importance of wind-blown snow redistri-  
1060 bution to snow accumulation on bellingshausen sea ice. *Annals of Glaciology*,  
1061 *52*(57), 271–278. doi: 10.3189/172756411795931651
- 1062 Li, L., & Pomeroy, J. W. (1997). Estimates of Threshold Wind Speeds for Snow  
1063 Transport Using Meteorological Data. *Journal of Applied Meteorology*, *36*(3),  
1064 205–213. doi: 10.1175/1520-0450(1997)036<0205:eotwsf>2.0.co;2
- 1065 Lindenmaier, I., Nelson, D., Isom, B., Hardin, J., Matthews, A., Wendler, T., &  
1066 Castro, V. (2020). *Ka arm zenith radar (kazrcfrge)*. (Atmospheric Radiation  
1067 Measurement (ARM) user facility.) doi: 10.5439/1498936
- 1068 Liston, G. E., & Elder, K. (2006a). A distributed snow-evolution modeling system  
1069 (snowmodel). *Journal of Hydrometeorology*, *7*(6), 1259–1276. Retrieved from  
1070 <https://doi.org/10.1175/JHM548.1> doi: 10.1175/JHM548.1
- 1071 Liston, G. E., & Elder, K. (2006b). A Meteorological Distribution System for High-  
1072 Resolution Terrestrial Modeling (MicroMet). *Journal of Hydrometeorology*,  
1073 *7*(2), 217–234. doi: 10.1175/jhm486.1
- 1074 Liston, G. E., Haehnel, R. B., Sturm, M., Hiemstra, C. A., Berezovskaya, S., &  
1075 Tabler, R. D. (2007). Simulating complex snow distributions in windy envi-  
1076 ronments using snowtran-3d. *Journal of Glaciology*, *53*(181), 241–256. doi:

- 1077 10.3189/172756507782202865
- 1078 Liston, G. E., Itkin, P., Stroeve, J., Tschudi, M., Stewart, J. S., Pedersen, S. H.,  
 1079 ... Elder, K. (2020). A lagrangian snow-evolution system for sea-ice ap-  
 1080 plications (snowmodel-1g): Part i—model description. *Journal of Geophys-*  
 1081 *ical Research: Oceans*, 125(10), e2019JC015913. Retrieved from [https://](https://agupubs.onlinelibrary.wiley.com/doi/abs/10.1029/2019JC015913)  
 1082 [agupubs.onlinelibrary.wiley.com/doi/abs/10.1029/2019JC015913](https://agupubs.onlinelibrary.wiley.com/doi/abs/10.1029/2019JC015913)  
 1083 (e2019JC015913 2019JC015913) doi: <https://doi.org/10.1029/2019JC015913>
- 1084 Liston, G. E., Polashenski, C., Rösel, A., Itkin, P., King, J., Merkouriadi, I., & Haa-  
 1085 pala, J. (2018). A distributed snow-evolution model for sea-ice applications  
 1086 (snowmodel). *Journal of Geophysical Research: Oceans*, 123(5), 3786–3810.  
 1087 Retrieved from [https://agupubs.onlinelibrary.wiley.com/doi/abs/](https://agupubs.onlinelibrary.wiley.com/doi/abs/10.1002/2017JC013706)  
 1088 [10.1002/2017JC013706](https://agupubs.onlinelibrary.wiley.com/doi/abs/10.1002/2017JC013706) doi: 10.1002/2017JC013706
- 1089 Liston, G. E., & Sturm, M. (1998). A snow-transport model for complex terrain.  
 1090 *Journal of Glaciology*, 44(148), 498–516. doi: 10.3189/S0022143000002021
- 1091 Macfarlane, A. R., Löwe, H., Gimenes, L., Wagner, D. N., Dadic, R., Ottersberg,  
 1092 R., ... Schneebeli, M. (2023). Thermal conductivity of snow on arctic sea  
 1093 ice. *EGUsphere*, 2023, 1–22. Retrieved from [https://egusphere.copernicus](https://egusphere.copernicus.org/preprints/egusphere-2023-83/)  
 1094 [.org/preprints/egusphere-2023-83/](https://egusphere.copernicus.org/preprints/egusphere-2023-83/) doi: 10.5194/egusphere-2023-83
- 1095 Macfarlane, A. R., Schneebeli, M., Dadic, R., Wagner, D. N., Arndt, S., Clemens-  
 1096 Sewall, D., ... Tavri, A. (2021). Snowpit SnowMicroPen (SMP) force  
 1097 profiles collected during the MOSAiC expedition [data set]. PANGAEA.  
 1098 Retrieved from <https://doi.org/10.1594/PANGAEA.935554> (In: Mac-  
 1099 farlane, AR et al. (2021): Snowpit raw data collected during the MOSAiC  
 1100 expedition. PANGAEA, <https://doi.org/10.1594/PANGAEA.935934>) doi:  
 1101 [10.1594/PANGAEA.935554](https://doi.org/10.1594/PANGAEA.935554)
- 1102 Mälicke, M. (2022). Scikit-gstat 1.0: a scipy-flavored geostatistical variogram esti-  
 1103 mation toolbox written in python. *Geoscientific Model Development*, 15(6),  
 1104 2505–2532. Retrieved from [https://gmd.copernicus.org/articles/15/](https://gmd.copernicus.org/articles/15/2505/2022/)  
 1105 [2505/2022/](https://gmd.copernicus.org/articles/15/2505/2022/) doi: 10.5194/gmd-15-2505-2022
- 1106 Matheron, G. (1963, 12). Principles of geostatistics. *Economic Geology*, 58(8), 1246-  
 1107 1266. Retrieved from <https://doi.org/10.2113/gsecongeo.58.8.1246> doi:  
 1108 [10.2113/gsecongeo.58.8.1246](https://doi.org/10.2113/gsecongeo.58.8.1246)
- 1109 Matrosov, S. Y. (2007). Modeling Backscatter Properties of Snowfall at Millimeter  
 1110 Wavelengths. *Journal of the Atmospheric Sciences*, 64(5), 1727–1736. doi: 10  
 1111 .1175/jas3904.1
- 1112 Matrosov, S. Y., Shupe, M. D., & Djalalova, I. V. (2008). Snowfall Retrievals Using  
 1113 Millimeter-Wavelength Cloud Radars. *Journal of Applied Meteorology and Cli-*  
 1114 *matology*, 47(3), 769–777. doi: 10.1175/2007jamc1768.1
- 1115 Matrosov, S. Y., Shupe, M. D., & Uttal, T. (2022, 04). High temporal resolution  
 1116 estimates of Arctic snowfall rates emphasizing gauge and radar-based retrievals  
 1117 from the MOSAiC expedition. *Elementa: Science of the Anthropocene*, 10(1).  
 1118 Retrieved from <https://doi.org/10.1525/elementa.2021.00101> (00101)  
 1119 doi: 10.1525/elementa.2021.00101
- 1120 Melo, D. B., Sharma, V., Comola, F., Sigmund, A., & Lehning, M. (2021). Modeling  
 1121 snow saltation: the effect of grain size and interparticle cohesion. *Earth and*  
 1122 *Space Science Open Archive*, 29. Retrieved from [https://doi.org/10.1002/](https://doi.org/10.1002/essoar.10507087.1)  
 1123 [essoar.10507087.1](https://doi.org/10.1002/essoar.10507087.1) doi: 10.1002/essoar.10507087.1
- 1124 Merkouriadi, I., Gallet, J.-C., Graham, R. M., Liston, G. E., Polashenski, C., Rösel,  
 1125 A., & Gerland, S. (2017). Winter snow conditions on arctic sea ice north of  
 1126 svalbard during the norwegian young sea ice (n-ice2015) expedition. *Journal*  
 1127 *of Geophysical Research: Atmospheres*, 122(20), 10,837–10,854. Retrieved  
 1128 from [https://agupubs.onlinelibrary.wiley.com/doi/abs/10.1002/](https://agupubs.onlinelibrary.wiley.com/doi/abs/10.1002/2017JD026753)  
 1129 [2017JD026753](https://agupubs.onlinelibrary.wiley.com/doi/abs/10.1002/2017JD026753) doi: 10.1002/2017JD026753
- 1130 Mott, R., Schirmer, M., Bavay, M., Grünwald, T., & Lehning, M. (2010). Un-  
 1131 derstanding snow-transport processes shaping the mountain snow-cover. *The*

- 1132 *Cryosphere*, 4(4), 545–559. Retrieved from <https://www.the-cryosphere>  
 1133 [.net/4/545/2010/](https://www.the-cryosphere.net/4/545/2010/) doi: 10.5194/tc-4-545-2010
- 1134 Nandan, V., Willatt, R., Mallett, R., Stroeve, J., Geldsetzer, T., Scharien, R., ...  
 1135 Hoppman, M. (2022). Wind transport of snow impacts ka- and ku-band radar  
 1136 signatures on arctic sea ice. *The Cryosphere Discussions*, 2022, 1–38. Re-  
 1137 trieved from <https://tc.copernicus.org/preprints/tc-2022-116/> doi:  
 1138 10.5194/tc-2022-116
- 1139 Nicolaus, M., Haas, C., Bareiss, J., & Willmes, S. (2006). A model study  
 1140 of differences of snow thinning on arctic and antarctic first-year sea ice  
 1141 during spring and summer. *Annals of Glaciology*, 44, 147–153. doi:  
 1142 10.3189/172756406781811312
- 1143 Nicolaus, M., Perovich, D., Spreen, G., Granskog, M., Albedyll, L., Angelopou-  
 1144 los, M., ... Wendisch, M. (2021). Overview of the mosaic expedition  
 1145 - snow and sea ice. *Elementa: Science of the Anthropocene*, 9. Re-  
 1146 trieved from <https://doi.org/10.1525/elementa.2021.000046> doi:  
 1147 10.1525/elementa.2021.000046
- 1148 Nixdorf, U., Dethloff, K., Rex, M., Shupe, M., Sommerfeld, A., Perovich, D. K., ...  
 1149 Boetius, A. (2021, September). *Mosaic extended acknowledgement*. Zen-  
 1150 odo. Retrieved from <https://doi.org/10.5281/zenodo.5541624> doi:  
 1151 10.5281/zenodo.5541624
- 1152 Persson, P. O. G. (2012). Onset and end of the summer melt season over sea ice:  
 1153 thermal structure and surface energy perspective from SHEBA. *Climate Dy-*  
 1154 *namics*, 39(6), 1349–1371. doi: 10.1007/s00382-011-1196-9
- 1155 Persson, P. O. G., Shupe, M. D., Perovich, D., & Solomon, A. (2017). Linking at-  
 1156 mospheric synoptic transport, cloud phase, surface energy fluxes, and sea-ice  
 1157 growth: observations of midwinter SHEBA conditions. *Climate Dynamics*,  
 1158 49(4), 1341–1364. doi: 10.1007/s00382-016-3383-1
- 1159 Petrich, C., Eicken, H., Polashenski, C. M., Sturm, M., Harbeck, J. P., Perovich,  
 1160 D. K., & Finnegan, D. C. (2012). Snow dunes: A controlling factor of melt  
 1161 pond distribution on arctic sea ice. *Journal of Geophysical Research: Oceans*,  
 1162 117(C9). Retrieved from [https://agupubs.onlinelibrary.wiley.com/doi/](https://agupubs.onlinelibrary.wiley.com/doi/abs/10.1029/2012JC008192)  
 1163 [abs/10.1029/2012JC008192](https://doi.org/10.1029/2012JC008192) doi: <https://doi.org/10.1029/2012JC008192>
- 1164 Pomeroy, J. W., & Gray, D. M. (1990). Saltation of snow. *Water Resources Re-*  
 1165 *search*, 26(7), 1583-1594. Retrieved from [https://agupubs.onlinelibrary](https://agupubs.onlinelibrary.wiley.com/doi/abs/10.1029/WR026i007p01583)  
 1166 [.wiley.com/doi/abs/10.1029/WR026i007p01583](https://doi.org/10.1029/WR026i007p01583) doi: [https://doi.org/](https://doi.org/10.1029/WR026i007p01583)  
 1167 [10.1029/WR026i007p01583](https://doi.org/10.1029/WR026i007p01583)
- 1168 Schlögl, S., Marty, C., Bavay, M., & Lehning, M. (2016). Sensitivity of alpine3d  
 1169 modeled snow cover to modifications in dem resolution, station coverage and  
 1170 meteorological input quantities. *Environmental Modelling Software*, 83, 387-  
 1171 396. Retrieved from [https://www.sciencedirect.com/science/article/](https://www.sciencedirect.com/science/article/pii/S1364815216300378)  
 1172 [pii/S1364815216300378](https://doi.org/10.1016/j.envsoft.2016.02.017) doi: <https://doi.org/10.1016/j.envsoft.2016.02.017>
- 1173 Schmidt, J. (2014). *terrainblockmesher*. GitHub. Retrieved from [https://](https://github.com/jonasIWES/terrainBlockMesher)  
 1174 [github.com/jonasIWES/terrainBlockMesher](https://github.com/jonasIWES/terrainBlockMesher) (IWESOL - IWES Open Li-  
 1175 brary, Fraunhofer IWES, Oldenburg, Germany)
- 1176 Schmidt, R. A. (1980). Threshold wind-speeds and elastic impact in snow transport.  
 1177 *Journal of Glaciology*, 26(94), 453–467. doi: 10.3189/S0022143000010972
- 1178 Schneebeli, M., & Johnson, J. B. (1998). A constant-speed penetrometer for high-  
 1179 resolution snow stratigraphy. *Annals of Glaciology*, 26, 107–111. doi: 10.3189/  
 1180 1998AoG26-1-107-111
- 1181 Selige, T., Böhner, J., & Ringeler, A. (2006, 01). Processing of srtm x-sar data to  
 1182 correct interferometric elevation models for land surface applications. *Göttinger*  
 1183 *Geographische Abhandlungen*, 115.
- 1184 Sharma, V., Braud, L., & Lehning, M. (2019). Understanding snow bedform for-  
 1185 mation by adding sintering to a cellular automata model. *The Cryosphere*,  
 1186 13(12), 3239–3260. Retrieved from <https://www.the-cryosphere.net/13/>

- 1187 3239/2019/ doi: 10.5194/tc-13-3239-2019
- 1188 Shupe, M., Chu, D., Costa, D., Cox, C., Creamean, J., de Boer, G., ... Wagner, D.  
1189 (2021, 6). Multidisciplinary drifting observatory for the study of arctic climate  
1190 (mosaic) (field campaign report). Retrieved from [https://www.osti.gov/  
1191 biblio/1787856](https://www.osti.gov/biblio/1787856) doi: 10.2172/1787856
- 1192 Shupe, M., Rex, M., Blomquist, B., Persson, P., Schmale, J., Uttal, T., ... Yue, F.  
1193 (2022). Overview of the mosaic expedition—atmosphere. *Elementa: Science of  
1194 the Anthropocene*, 10(1). doi: 10.1525/elementa.2021.00060
- 1195 Steger, C. R., Reijmer, C. H., van den Broeke, M. R., Wever, N., Forster, R. R.,  
1196 Koenig, L. S., ... Noël, B. P. Y. (2017). Firn meltwater retention on the  
1197 greenland ice sheet: A model comparison. *Frontiers in Earth Science*, 5,  
1198 3. Retrieved from [https://www.frontiersin.org/article/10.3389/  
1199 feart.2017.00003](https://www.frontiersin.org/article/10.3389/feart.2017.00003) doi: 10.3389/feart.2017.00003
- 1200 Sturm, M., & Holmgren, J. (2018). An Automatic Snow Depth Probe for Field Val-  
1201 idation Campaigns. *Water Resources Research*, 54(11), 9695–9701. doi: 10  
1202 .1029/2018wr023559
- 1203 Sturm, M., Holmgren, J., & Perovich, D. K. (2002). Winter snow cover on the  
1204 sea ice of the arctic ocean at the surface heat budget of the arctic ocean  
1205 (sheba): Temporal evolution and spatial variability. *Journal of Geophysical  
1206 Research: Oceans*, 107(C10), SHE 23-1-SHE 23-17. Retrieved from [https://  
1207 agupubs.onlinelibrary.wiley.com/doi/abs/10.1029/2000JC000400](https://agupubs.onlinelibrary.wiley.com/doi/abs/10.1029/2000JC000400) doi:  
1208 10.1029/2000JC000400
- 1209 Sturm, M., & Massom, R. A. (2016). Snow in the sea ice system: friend or foe?  
1210 In *Sea ice* (p. 65-109). John Wiley and Sons, Ltd. Retrieved from [https://  
1211 onlinelibrary.wiley.com/doi/abs/10.1002/9781118778371.ch3](https://onlinelibrary.wiley.com/doi/abs/10.1002/9781118778371.ch3) doi: 10  
1212 .1002/9781118778371.ch3
- 1213 Sullivan, C. B., & Kaszynski, A. (2019, May). PyVista: 3D plotting and mesh anal-  
1214 ysis through a streamlined interface for the Visualization Toolkit (VTK). *Jour-  
1215 nal of Open Source Software*, 4(37), 1450. Retrieved from [https://doi.org/  
1216 10.21105/joss.01450](https://doi.org/10.21105/joss.01450) doi: 10.21105/joss.01450
- 1217 Vosselman, G. (2000, 01). Slope based filtering of laser altimetry data. *IAPRS*,  
1218 XXXIII.
- 1219 Wagner, D. N., & Frey, M. M. (2023, March). *Preliminary data of drifting snow  
1220 mass flux from the lower SPC at MOSAiC (2020-01-26 to 2020-02-04) for the  
1221 submitted paper "Towards a fully physical representation of snow on Arctic sea  
1222 ice using a 3D snow-atmosphere model"* [dataset]. Zenodo. Retrieved from  
1223 <https://doi.org/10.5281/zenodo.7715728> doi: 10.5281/zenodo.7715728
- 1224 Wagner, D. N., Jaggi, M., Macfarlane, A. R., Arndt, S., Krampe, D., Regnery, J., ...  
1225 Schneebeli, M. (2021). *Snow water equivalent retrievals from snowmicropen  
1226 data from mosaic leg 1 - leg 3*. (PANGAEA) doi: 10.1594/PANGAEA.927460
- 1227 Wagner, D. N., & Lehning, M. (2023, March). *Preliminary DOI/Repository of  
1228 ALPINE3D and SNOWPACK data of the submitted paper "Towards a fully  
1229 physical representation of snow on Arctic sea ice using a 3D snow-atmosphere  
1230 model"* [dataset]. Zenodo. Retrieved from [https://doi.org/10.5281/  
1231 zenodo.7723224](https://doi.org/10.5281/zenodo.7723224) doi: 10.5281/zenodo.7723224
- 1232 Wagner, D. N., Shupe, M. D., Cox, C., Persson, O. G., Uttal, T., Frey, M. M.,  
1233 ... Lehning, M. (2022). Snowfall and snow accumulation during the mo-  
1234 saic winter and spring seasons. *The Cryosphere*, 16(6), 2373–2402. Re-  
1235 trieved from [https://tc.copernicus.org/articles/16/2373/2022/  
1236 10.5194/tc-16-2373-2022](https://tc.copernicus.org/articles/16/2373/2022/) doi:
- 1237 Webster, M. A., Rigor, I. G., Nghiem, S. V., Kurtz, N. T., Farrell, S. L., Perovich,  
1238 D. K., & Sturm, M. (2014). Interdecadal changes in snow depth on ar-  
1239 ctic sea ice. *Journal of Geophysical Research: Oceans*, 119(8), 5395–5406.  
1240 Retrieved from [https://agupubs.onlinelibrary.wiley.com/doi/abs/  
1241 10.1002/2014JC009985](https://agupubs.onlinelibrary.wiley.com/doi/abs/10.1002/2014JC009985) doi: <https://doi.org/10.1002/2014JC009985>

- 1242 Weiss, A. I., King, J., Lachlan-Cope, T., & Ladkin, R. (2011). On the effective  
1243 aerodynamic and scalar roughness length of weddell sea ice. *Journal of Geo-*  
1244 *physical Research: Atmospheres*, *116*(D19). Retrieved from <https://agupubs>  
1245 [.onlinelibrary.wiley.com/doi/abs/10.1029/2011JD015949](https://agupubs.onlinelibrary.wiley.com/doi/abs/10.1029/2011JD015949) doi: 10.1029/  
1246 2011JD015949
- 1247 Weller, H. G., Tabor, G., Jasak, H., & Fureby, C. (1998). A tensorial approach to  
1248 computational continuum mechanics using object-oriented techniques. *Comput-*  
1249 *ers in Physics*, *12*(6), 620. doi: 10.1063/1.168744
- 1250 Wever, N., Leonard, K., Maksym, T., White, S., Proksch, M., & Lenaerts, J. T. M.  
1251 (2021). Spatially distributed simulations of the effect of snow on mass balance  
1252 and flooding of antarctic sea ice. *Journal of Glaciology*, *67*(266), 1055–1073.  
1253 doi: 10.1017/jog.2021.54
- 1254 Wever, N., Rossmann, L., Maaß, N., Leonard, K. C., Kaleschke, L., Nicolaus, M.,  
1255 & Lehning, M. (2020). Version 1 of a sea ice module for the physics-based,  
1256 detailed, multi-layer snowpack model. *Geoscientific Model Development*, *13*(1),  
1257 99–119. Retrieved from <https://www.geosci-model-dev.net/13/99/2020/>  
1258 doi: 10.5194/gmd-13-99-2020
- 1259 Widener, K., Bharadwaj, N., & Johnson, K. (2012). *Ka-Band ARM Zenith Radar*  
1260 *(KAZR) Handbook*. (Tech. Rep.). (ARM user facility. DOE/SC-ARM/TR-  
1261 106.)
- 1262 Zhang, W., Qi, J., Wan, P., Wang, H., Xie, D., Wang, X., & Yan, G. (2016). An  
1263 easy-to-use airborne lidar data filtering method based on cloth simulation. *Re-*  
1264 *mote Sensing*, *8*(6). Retrieved from [https://www.mdpi.com/2072-4292/8/6/](https://www.mdpi.com/2072-4292/8/6/501)  
1265 501 doi: 10.3390/rs8060501